Chemical Science



EDGE ARTICLE

View Article Online



Cite this: Chem. Sci., 2021, 12, 1693

d All publication charges for this article have been paid for by the Royal Society of Chemistry

Received 8th November 2020 Accepted 8th December 2020

DOI: 10.1039/d0sc06157c

rsc.li/chemical-science

Fast reversible isomerization of merocyanine as a tool to quantify stress history in elastomers†

Yinjun Chen, (1) ‡a C. Joshua Yeh, (10) §a Qiang Guo, b Yuan Qi, b Rong Long (10) b and Costantino Creton (1)**

A mechanochemistry based approach is proposed to detect and map stress history during dynamic processes. Spiropyran (SP), a force sensitive molecular probe, was incorporated as a crosslinker into multiple network elastomers (MNE). When these mechanochromic MNEs are loaded, SP undergoes a well-known force-activated reaction to merocyanine (MC) changing its absorption in the visible range (visible blue color). This SP to MC transition is not reversible within the time frame of the experiment and the color change reports the concentration of activated molecules. During subsequent loadingunloading cycles the MC undergoes a fast and reversible isomerization resulting in a slight shift of absorption spectrum and results in a second color change (blue to purple color corresponding to the loading-unloading cycles). Quantification of the color changes by using chromaticity shows that the exact color observed upon unloading is characteristic not only of the current stress (reported by the shift in color due to MC isomerization), but of the maximum stress that the material has seen during the loading cycle (reported by the shift in color due to the change in MC concentration). We show that these two color changes can be separated unambiguously and we use them to map the stress history in the loading and unloading process occurring as a crack opens up and propagates, breaking the material. Color maps on fractured samples are compared with finite element simulations and the agreement is excellent.

Introduction

Although soft and elastic materials are found in many industrial applications, predicting their strength from their molecular structure remains difficult in particular because there are few tools to characterize damage and fracture at the molecular scale. Hence materials design relies still on empirical methods. In particular the extent of damage of an elastomer is currently modeled with fully phenomenological methods and no feedback can be given to materials designers to make the materials structure more damage resistant. Such a feedback can only be given if physically based models are developed and such models require experimental data to be calibrated.

One of the major recent advances to characterize the mechanical properties of polymeric materials at the molecular level has been the development of force-sensitive mechanophore molecules that exhibit mechanically activated optical responses, such as light emission (luminescence),1 color changes² and fluorescence³ in response to the application of a mechanical force to a specific chemical bond. When these molecules are incorporated in the polymer network in a loadbearing position, they can be activated and respond locally to the application of a stress on a macroscopic sample, making it therefore possible to spatially map the optical activation. These responses have mainly been used to qualitatively investigate the mechanical properties of materials,4 the interactions between different interfaces,5 the damage zone around a crack tip,6 and the tailoring of physical properties.7 Only a few studies8 focused on the actual quantification of the mechanically activated optical signals, which is needed to understand how stresses and strains are distributed to molecules and to develop physically based constitutive models.

One of the reasons is that mechanophore molecules are currently not commercially available and need to be incorporated into the materials with a suitable synthetic method, which is specific for each new material. Furthermore the technique competes with the versatile digital image correlation (DIC)9 and particle tracking10 techniques, that are able to quantitatively

[&]quot;Laboratory of Soft Matter Science and Engineering, ESPCI Paris, PSL University, CNRS, Sorbonne Université, 75005 Paris, France. E-mail: costantino.creton@espci. psl.eu

^bDepartment of Mechanical Engineering, University of Colorado Boulder, Boulder, CO, 80309 USA

available. information (ESI) DOI: † Electronic supplementary 10.1039/d0sc06157c

[‡] Current address: Department of Chemical Engineering & Chemistry and Institute for Complex Molecular Systems, Eindhoven University of Technology, 5600 MB Eindhoven, Netherlands

[§] Current address: 3M research center, St-Paul, MN, USA.

detect the strain field with high accuracy in many situations¹¹ without any chemical labeling of the material.

Although mechanophores still provide less quantitative information than DIC for the time being, they allow direct optical visualization of the spatially resolved level of activation. Recently, Xia et al. 12 incorporated mechanochromic spiropyran based (SP) molecules as crosslinkers into Sylgard 184 (an elastomer containing nanofillers) and demonstrated their usefulness for mapping strains in fast impact experiments. A color change due to the activation of SP into merocyanine (MC) was observed during the deformation of the materials and the distribution of color change was qualitatively consistent with the prediction of Von Mises strain fields by finite element analysis suggesting that activation is caused by an average level of strain. Park et al. 13 also incorporated SP into a nanocomposite with pores and silica nanoparticles and observed color changes with increasing strain. With their particular material they observed enhanced activation even at moderate stress, a useful property for responsive electronic skin elastomers. However, the complex structure of the materials makes it difficult to directly connect molecular activation and strains.

If strain fields can be mapped by DIC, detecting stress is much more difficult and this is where mechanophores can have an edge. If DIC is used, a constitutive model is needed to calculate the stress field from the strain field. For soft polymer networks, many constitutive models have been proposed and are used such as the neo-Hookean model, the Mooney–Rivlin model,¹⁴ Ogden's model,¹⁵ Gent's model.¹⁶ Although these models fit the data well in uniaxial extension, they are often not validated by direct experimental evidence in other geometries involving multiaxial loading. In addition, when strainhardening materials are deformed to large strains such as near fracture points, the displacement measurement obtained from DIC and particle tracking becomes inaccurate and result in large uncertainties in the stresses predicted by the assumed constitutive modeling.

Motivated by this fact, in a previous work¹⁷ we quantified the color changes of multiple network elastomers (MNEs) containing SP undergoing uniaxial tension. We demonstrated that the color of the sample was directly proportional to the concentration of activated SP in the material. By constructing a calibration curve between color change and nominal stress during loading, the stress field around a crack tip prior to propagation was quantitatively mapped and the results were validated with finite element simulations. This quantification work was however limited to mapping the stress evolution during loading by the force-activated transition between SP and merocyanine (MC). As we argued in our previous work the observed color change is due to an increase in concentration of MC as the macroscopic load on the sample increases. Yet the forceinduced SP \rightarrow MC transition is not reversible within the time scale of the experiment so that the concentration of MC in the sample is only dependent on the maximum stress seen by the sample and does not change if the load is removed. Yet it would be very helpful to map stresses in dynamic experiments where materials can be locally loaded, damaged and then unloaded such as in the case of the propagation of a crack. For this

situation DIC does not give a unique answer for the stress (because of near crack tip damage during loading).

Craig et al.^{2d} incorporated SP as a crosslinker in a PDMS elastomer and observed a change in color from transparent (before force-activation) to blue (upon loading) to purple (upon full unloading). From the molecular point of view, the instantaneous and fully reversible color change during unloading and reloading was attributed to the isomerization of MC as shown in Fig. 1a. Namely, there are no less than two isomers of MC corresponding to the loading and unloading,¹⁸ respectively. In other words the MC concentration does not change upon unloading and reloading but the relative proportion of the two isomers has a force dependent equilibrium with a very low activation energy.

Weng *et al.*¹⁹ also used this color change to demonstrate unloading around the crack tip during the propagation of a crack in polyurethane illustrating that the two-color change is sensitive to the change in stress in the materials. However, their approach was not quantitative.

The purpose and novelty of this paper is to extend the quantitative color analysis approach of Chen *et al.*¹⁷ to two additional mechanical situations involving the application of a decreasing load:

- (1) The optical quantitative mapping of the maximum stress seen by the material point near the fracture plane measured post-mortem.
- (2) The optical quantitative mapping in a time-resolved way of the propagation of a crack including in the regions unloaded by the propagation of the crack.

Both measurements are essential to calibrate and improve analytical and computational mechanical models to predict crack propagation in particular when the material is extensively damaged before failing.

To do that, we incorporate SP-based crosslinkers in ethyl acrylate-based multiple network elastomers^{6b,20} (MNE) following a previously developed synthetic procedure. Unlike PU, the MNEs exhibit no measurable viscoelasticity in uniaxial deformation and are sufficiently tough to activate a detectable amount of SP into MC upon loading. Hence, MNE are good model systems. After proper calibration, a direct measure of the change in local color (due to the isomerization of MC) with a simple RGB camera will be carried out on a propagating crack and on fracture surfaces. The experimental results will then be compared with finite element simulations to check the validity of this novel quantitative and time-resolved approach.

Results

Synthesis of mechanochromic multiple network elastomers and characterization of their mechanical properties

As previously reported, ^{6b,20,21} MNEs consist of a more highly crosslinked first network (the filler network) interpenetrated with one or more less crosslinked network(s) (the matrix networks), synthesized by sequences of monomer swelling and free radical polymerization. The filler network was prepared by UV photopolymerizing a mixture of ethyl acrylate (EA) monomers, spiropyran (SP) and 1,4-butanediol diacrylate (BDA)

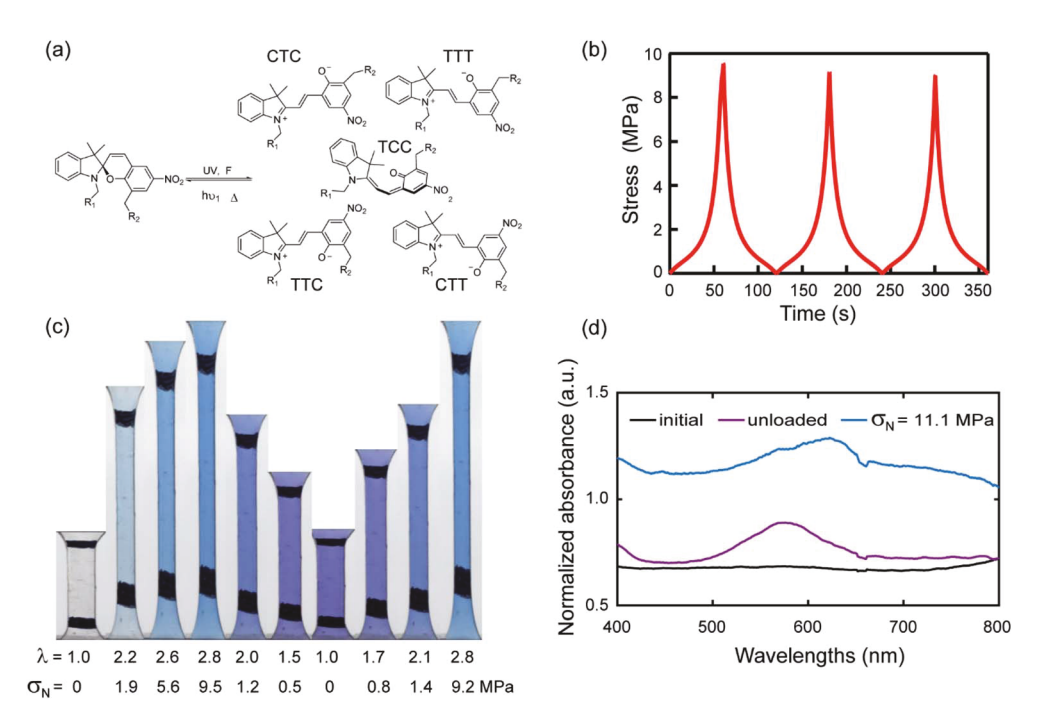


Fig. 1 (a) Schematic representation of different isomers of MC; (b) stress—time curve of EA0.2-0.05(2.61) in a three-cycle extension test. (c) Images of EA0.2-0.05(2.61) for one and a half cycle in loading, unloading and reloading process; (d) UV-vis absorption spectra of EA0.2-0.05(2.61) in two different situations.

crosslinkers, and 2-hydroxy-2-methylpropiophenone (HMP) initiator. Since the crosslinking and entanglement structure of the filler network controls the stiffness and extensibility of the MNEs^{6b,20,21} we prepared networks with two crosslinking concentrations of 0.5 mol% and 0.2 mol% relative to EA monomers at a constant SP concentration. The composition used to prepare the much less crosslinked matrix networks was made of EA, 0.01 mol% BDA and 0.01 mol% HMP relative to EA monomers (see Section S1 of the ESI† for details of the synthesis). In the following, each sample is named Ax-y(z), where A, x, y, z denote the monomer, crosslinker concentration, SP concentration, and isotropic prestretch from swelling of the filler network. The detailed information on materials properties is shown in Table 1. All the data are measured in uniaxial extension at a stretch rate of 0.05 s⁻¹.

While a significant improvement in stiffness and fracture toughness was observed for both families of materials

 $\begin{tabular}{lll} {\bf Table} & {\bf 1} & {\bf Mechanical} & {\bf properties} & {\bf of} & {\bf various} & {\bf multiple} & {\bf network} \\ {\bf elastomers}^a & & & \\ \hline \end{tabular}$

λ_0	E (MPa)	σ_{m} (MPa)	(λ_b)	
1	0.62	0.86	4.1	
1.70	0.90	10	4.2	
2.61	1.24	11.3	3.1	
1	0.85	1.1	2.1	
1.56	1.16	4.6	2.5	
2.23	1.88	15.7	2.7	
	1 1.70 2.61 1 1.56	1 0.62 1.70 0.90 2.61 1.24 1 0.85 1.56 1.16	1 0.62 0.86 1.70 0.90 10 2.61 1.24 11.3 1 0.85 1.1 1.56 1.16 4.6	

 $[^]a$ $λ_0$: pre-stretch of filler network, E: Young's modulus, $σ_m$: nominal stress at break, $λ_b$: stretch at break.

consistent with results reported in previous work^{6b,20,21} (Fig. S1[†] and Table 1), the more highly prestretched elastomers (EA0.5-0.05(2.23) and EA0.2-0.05(2.61)) with the highest Young's modulus and failure stress were selected for our experiments to maximize SP activation before fracture.

Mechanical response-color change in cyclic loading

To illustrate the reversible mechanochromic properties of the materials, the EA0.2-0.05(2.61) material was subjected to loading–unloading cycles in uniaxial extension and example results are summarized in Fig. 1. Stress–time data is shown in Fig. 1b for three cycles of loading–unloading. Fig. 1c shows images of the same sample for one and a half cycle to $\lambda=2.8$. The initially transparent (colorless) sample becomes blue during loading because of the force-activated conversion of SP into MC (an irreversible reaction within the time frame of the experiment) and purple during unloading, qualitatively consistent with previous studies on other materials. ^{2d,19} The second (and fast reversible within the time frame of the experiment) color change can be attributed to the coexistence of different isomers of merocyanine (MC) as shown in Fig. 1a. ^{2e}

To characterize more precisely the two-color changes, a UV-vis absorption spectrum was obtained for the EA0.2-0.5(2.61) samples during cyclic loading tests. In Fig. 1d, the absorption spectrum of the loaded sample (blue curve) presents a broad peak between the wavelength of 600 and 650 nm during loading. When the sample was fully unloaded, the absorption peak shifted to 580 nm (purple line). According to Wohl $et\ al.$, 22 different stable isomers have different characteristic absorption

peaks in the visible light region and thus result in different colors. The conversion from one absorption peak to another during loading and unloading validates the probable shift between two main isomers of MC reverting into each other during the cyclic loading test. Based on the computational work of Craig et al.,2e the SP derivative used in this work mainly transforms into five isomers as shown in Fig. 1a. Since these isomers are sensitive to stress and are able to transform into each other reversibly over the time scale of the loading/ unloading experiment, once the SP is activated into MC, the materials reversibly and instantaneously shift between different colors in response to the change in stress as shown in Fig. 1c. EA0.2-0.05(2.61) samples gradually shift from blue color into purple with decreasing applied stress. This suggests that the exact color may be directly related to the level of stress in the material, giving us therefore in principle the ability to quantify the stress during the unloading process.

Although the exact nature of the main isomers presents during loading and unloading cannot be ascertained, this does not matter for the quantification of stress as long as the respective stability of the isomers is sensitive to the stress level in the same way.

Construction of the 3D color-stress map and quantification

After presenting this example we now proceed to a systematic quantification to establish a calibration map. Fig. 2a shows stress–stretch data for a step cyclic loading performed on EA0.2-

0.05(2.61) samples at increasing values of λ_{max} . Note that the EA0.2-0.05(2.61) samples exhibit an excellent reversible elasticity up to an extension of $\lambda \sim 1.7$ and loading at different strain rates had little effect on the results, indicating that viscoelasticity can be ignored. When σ_N reaches 3 MPa in the third cycle, a mechanical hysteresis becomes observable, which suggests an initiation of damage (random bond scission) occurring in the materials. The hysteresis for each cycle and the total hysteresis were calculated as shown in Fig. S3.† Due to the weak C-O bond in SP, SP is activated (on average) prior to the onset of damage as shown in Fig. 2b and in Fig. S3[†] since an obvious color change is visible in the third cycle before mechanical hysteresis is detected. More SP are then activated with increasing maximum stretch resulting in the progressive increase in chromaticity in step cycle loading tests not only for the loaded sample but also for the unloaded samples ($\lambda = 1$) where the shade of purple becomes more intense as λ_{max} increases.

To quantify these changes in color, an RGB analysis based on color chromaticity was carried out for the step cyclic loading. Chromaticity relates to the intensity of specific color channels, *i.e.* red, green and blue. S_{ratio} , is defined as the ratio of the intensity of a color channel in eqn (1):

$$S_{\rm ratio} = \frac{S_{\rm i}}{\sum S_{\rm i}} \tag{1}$$

where $\sum S_i$ represent the summation of intensities of all the color channels and S_i represents the intensity of red, green and blue respectively. The chromatic change, ΔS_{ratio} , is then

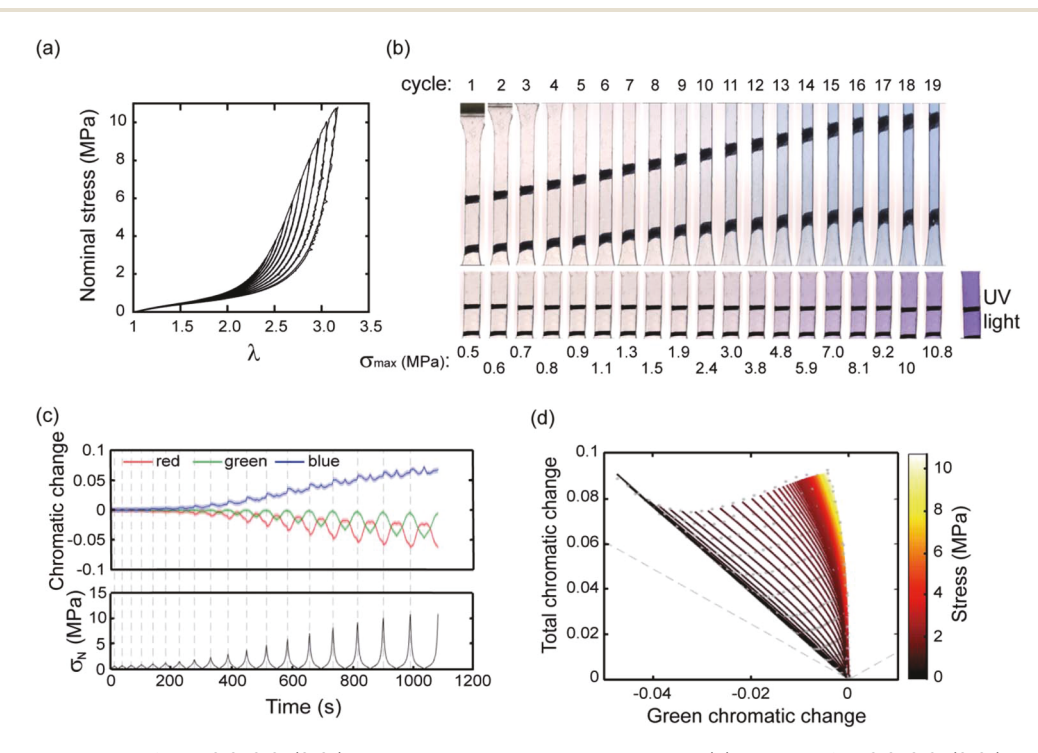


Fig. 2 (a) Stress-strain curve of a EA0.2-0.05(2.61) sample in a step cyclic loading test; (b) images of EA0.2-0.05(2.61) at the minimum and maximum deformation in the same step cyclic loading test; (c) chromatic change curve of EA0.2-0.05(2.61) sample in step cyclic loading test; (d) 3D color-stress map of the EA0.2-0.05(2.61) sample. The black dots are the experimental points and the green curves are the fitted curves for the relaxation. The color coding represents the nominal stress level. The grey dashed line corresponds to the boundary of physical meaningful chromatic coordinates.

Edge Article Chemical Science

calculated relative to the values measured at the beginning of the extension test.17 The chromaticity of the three color channels evolves with each loading/unloading cycle but also with cycle number since the maximum stress is progressively increased (Fig. 2c). As shown in Fig. 2c, the blue chromatic change shows two peaks at the maximum and minimum stress of each cycle, respectively. When the chromatic change is plotted as a function of σ_N during the unloading process, a change in chromaticity is not observed in the blue and red channels until σ (nominal stress) decreases below 2.5 MPa (see Fig. S4†). However, the green chromatic change is more sensitive to unloading. In other words, during the loading the SP irreversibly (within the time frame of the experiment) reverts to MC and the sample becomes blue, while during unloading the MC reverts instantaneously and reversibly to one of its isomers when it is unloaded. The intensity of the purple color depends however on the concentration of SP that was initially reverted into MC, which in turn depends on the maximum nominal stress that the sample has seen. Therefore, based on the observed color it should be in principle possible to identify both the actual value of σ_N and the maximum value of σ_N that this particular sample has seen.

To improve the sensitivity of chromatic changes to stress and the detection limit, a total chromatic change was defined. The total chromatic change, $\Delta T_{\rm ratio}$, was calculated based on the Euclidean norm:

$$\Delta T_{\rm ratio} = \sqrt{\Delta R_{\rm ratio}^2 + \Delta G_{\rm ratio}^2 + \Delta B_{\rm ratio}^2}$$
 (2)

The total and green chromatic changes were selected as parameters to visually separate the loading and unloading by associating the loading and unloading along the y and x axes of Fig. 2d, respectively. However, in principle, any two chromatic descriptors can be selected to fully describe the color state (see Section S2 of the ESI† for more details). A 3D colorstress map can be plotted, where coordinates on the color plane are assigned a nominal stress value. Color coded to stress lines as a function of green and total chromatic change are shown in Fig. 2d. The right edge of the map shows the stress curve during the loading of a virgin sample where SP changes into MC. The left part of the map corresponds to relaxation and reloading. Note that the color change during reloading retraces the unloading curves, indicating the reversibility between blue and purple. This result is consistent with the observation that the unloading and reloading curves in the stress-extension response overlap in Fig. 2a. This colorstress calibration map can then be used to measure the magnitude of the stress for each pixel in the sample region of an image during both the loading and unloading process. Since the concentration of MC in the sample (all isomers included) is only dependent on the maximum stress that the sample has seen, this information can be deduced from the chromatic change coordinates.

We will now examine how this mechanochemical approach can be used to investigate a fully macroscopic solid mechanics problem: the propagation of a crack in a sample from an initial notch. As the crack propagates the material points that were initially loaded in front of the crack tip, become progressively unloaded. This information that is currently impossible to obtain experimentally by any other method, is important to estimate the real energy release rate and the stress history of the sample.

Quantification of stress during the propagation of a crack

Fig. 3 shows a single edge notched rectangular sample (SEN) of EA0.2-0.05(2.61) being stretched monotonously at a constant stretch rate $\lambda = 0.05~\text{s}^{-1}$. When the stretch exceeds a critical value, the crack catastrophically propagates and the sample fails. The calibration map can be used to map a scalar representation of the principal components of the stress around the crack tip during crack propagation.17 A color camera (capturing at a rate of 30 frames per second) records the evolution of the color change around a crack tip during the test. Because of the fast crack velocity, only two frames were captured during the propagation process. As shown in Fig. 3a, color around the crack tip gradually changes into a deep blue from frames I to IV before the propagation of the crack starts. During the fast propagation, one of the frames was captured as shown in Fig. 3a (frame VI). Although frames taken during propagation are slightly blurry, regions of deep blue and purple are clearly visible and the color distribution on both sides of the crack tip are approximately symmetrical. As discussed above, the purple regions suggest a shift in the distribution between the isomeric MC populations due to unloading. A detailed color analysis was performed on each frame in order to create a pixel by pixel stress map of the loaded and unloaded regions. Note that the large difference in crack opening between frame V and frame VI with only a small change in λ is due to the fact that the stretch is measured far from the tip. An actual video of the propagation is

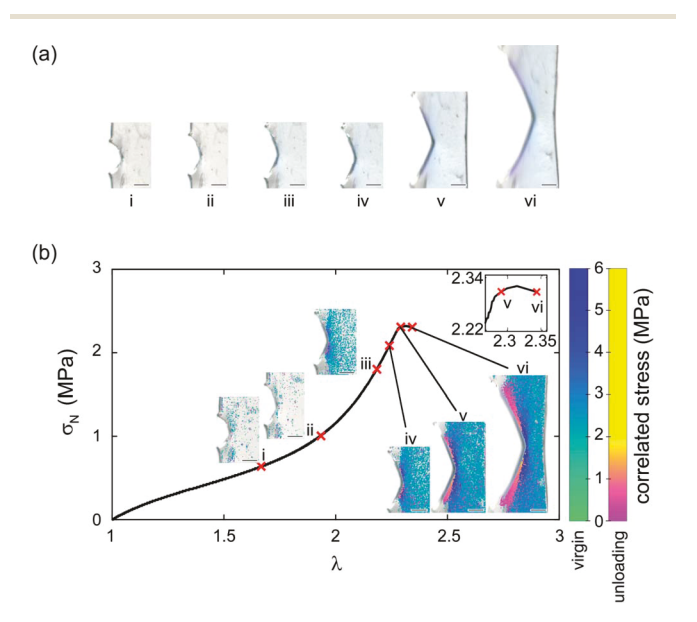


Fig. 3 (a) Image of EA0.2-0.05(2.61) during crack propagation; (b) stress map of the image in (a). The scale bar in the images represents 0.5 mm.

shown in ESI Movie S1† and similar images are available for the EA0.5-0.05(2.23) samples in Section S3 of the ESI.†

The calibration color-stress map of Fig. 2d can then be used to detect the spatial position of the unloaded regions of the sample, the 2D maps of the values of the local stress σ_{loc} during the loading of the SEN sample and the propagation of the crack are shown in Fig. 3b for different macroscopic values of tensile stretch and nominal stress. Around the peak macroscopic stress two regions in the shape of wedges where the material is unloaded are clearly visible (images V and VI). The unloaded regions start from the areas that exhibit the maximum stress concentration around the crack tip before crack propagation, gradually extending to areas further away from the crack as shown in Fig. 3b. This is the first time that the stress relaxation in the dynamic process of crack propagation is observed and quantified. In unloaded areas, the magnitude of the relaxation of stress increases with distance away from the crack tip (right to left) as shown in frame VI in Fig. 3b. The stress in the unloaded areas almost relaxes to 0. Note that crack propagation, starts to occur before the peak stress when most of the material is still under load. This is also an interesting result with potential practical relevance since it is notoriously difficult to identify exactly when the crack starts to propagate. By default the peak average stress (measured with the load cell far from the sample) is often used to determine Γ_c but our results show that this may not be true and that the crack may propagate before.

Post mortem analysis of the loading history

Although with our current standard camera we could not follow in detail the evolution of the stress map during the fast propagation, the samples could also be imaged post-mortem to determine in the fully unloaded state, the concentration of MC in the sample (reflecting the maximum stress seen by the sample) as a function of position from the fracture surface. This information is very useful to compare experimental results to FE modeling of crack growth.

From the chromatic change after failure, the maximum stress of each pixel can be extracted from the calibration color-stress map and hence the relationship between the distance away from the fracture plane and the maximum stress seen by that pixel, an information that can in principle be compared to modeling of crack propagation for multiple network elastomers. To validate the usefulness of this method, post mortem analysis was performed for EA0.2-0.05(2.61) and EA0.5-0.05(2.23), two materials made from different filler networks that exhibit a different strain stiffening behavior.

A schematic of the geometry of the sample is shown in Fig. 4a. The presence of a strong purple color near the fracture surface is observed, indicating a high level of SP activation (see also Fig. S20†). The intensity of the purple color decreases progressively with increasing distance away from the fracture surface.

Fig. 4b plots the peak stresses that the sample has seen in the uniaxial cyclic test as a function of the corresponding total

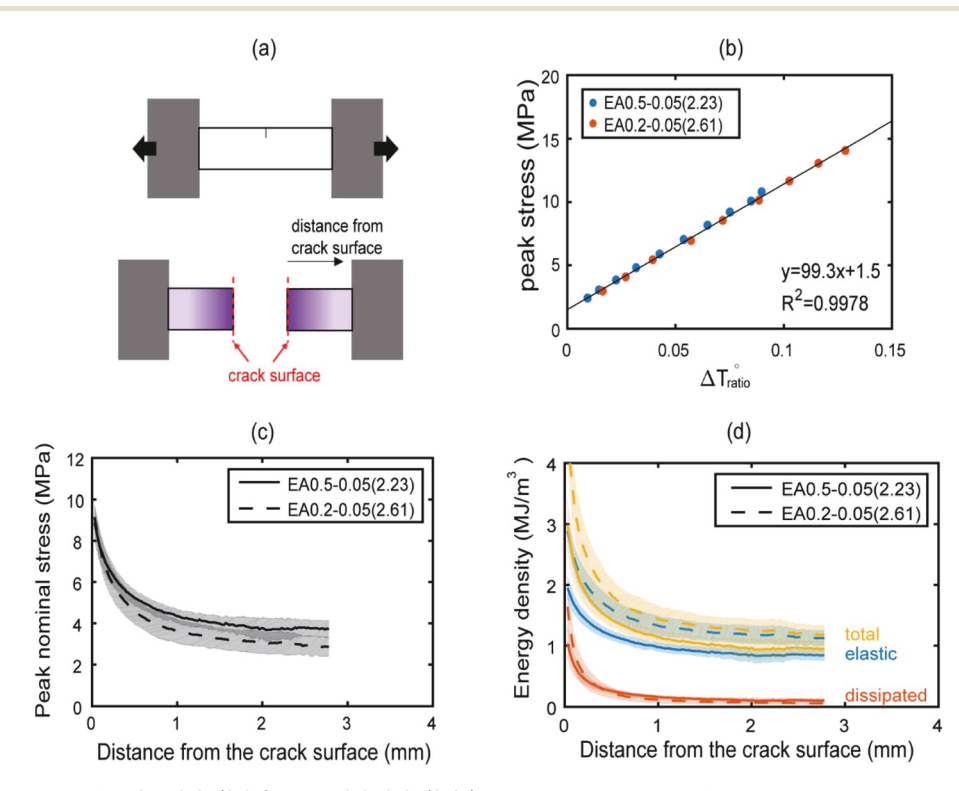


Fig. 4 Post mortem analysis of EA0.5-0.05(2.23) and EA0.2-0.05(2.61) samples. A schematic of a single edge notch sample pulled in tension (a). A schematic of a post mortem sample before and after the fracture test (b). The color changes were correlated with peak nominal stresses based on results from step cyclic tensile tests. The peak nominal stresses and energy densities are plotted as a function of normal distance from the crack edges in (c) and (d), respectively.

Edge Article Chemical Science

chromatic change, once the sample is back in the relaxed zero stress state for EA0.2-0.05(2.61). The same procedure was applied for the stiffer materials of EA0.5-0.05(2.23) and as expected¹⁷ the experimental points for the EA0.5-0.05(2.23) fall on the same straight line as those of the EA0.2-0.05(2.61) as shown in Fig. 4b, validating the feasibility to deduce maximum load from chromatic change after materials failure. The maximum stress distribution as a function of distance away from the edge is shown in Fig. 4c for both materials. EA0.2-0.05(2.61) shows a slightly lower peak nominal stresses at the same distance from the crack face compared to EA0.5-0.05(2.23). This is qualitatively consistent with the softer nature of the EA0.2-0.05(2.61) due to the lower crosslinker concentration in the filler network (see Fig. S3†).

Once the maximum stress information is extracted it is also possible to approximately separate the dissipated energy (through bond scission) from the released elastic energy. The dissipated energy density was calculated by integrating the hysteretic area in the cyclic stress-strain curves shown in Fig. 2a and S3a.† This allowed the construction of a calibration curve between the dissipated energy and the peak stress, which can then be used to create an averaged dissipated energy profile perpendicular to the crack edge, as shown in Fig. 4d. A detailed procedure of the analysis can be found in the ESI.† In Fig. 4d, the total and elastic energy densities for the softer EA0.2-0.05(2.61) materials both exhibited higher values than for the stiffer EA0.5-0.05(2.23) material reflecting the reduction in crosslinker concentration in the filler network and the larger extensibility of the filler network. For regions close to the edge, the dissipated energy density for the soft material is larger than for the stiff material, which is consistent with the idea that a larger dissipated energy region leads to a higher fracture toughness.

Simulation of crack propagation

The measured stress history can provide critical inputs for developing fracture models capable of simulating crack propagation in soft elastomers. To demonstrate this point, we built a FE model for the SEN sample of EA0.2-0.05(2.61) (see Fig. S21†). A constitutive model was developed to capture the nonlinear, hysteretic stress-strain relation in this material by fitting the cyclic uniaxial tension data in Fig. 2a (see Fig. S22a†). Moreover, we implemented a cohesive zone model to describe the fracture process at the crack tip, which required two key parameters: intrinsic fracture energy Γ_0 and cohesive strength $\sigma_{\rm c\ max}$ (Fig. S21†). It is a challenging task to calibrate these two parameters for soft elastomers due to the lack of sufficient understanding on the crack tip fracture process. We leveraged the post-mortem analysis, specifically the peak nominal stress distribution in Fig. 4c, to determine the cohesive parameters. First, $\sigma_{\rm c\ max}$ was set to be 11.3 MPa according to the nominal stress at break under macroscopic tension for EA0.2-0.05(2.61) (see Table 1), which is close to the maximum peak nominal stress observed in Fig. 4c. Second, Γ_0 was determined by fitting the peak nominal stress distribution (see Fig. S23†) and was found to be 4.6 kJ m^{-2} .

Using the calibrated FE model, we were able to simulate the crack propagation in EA0.2-0.05(2.61) (see Fig. 5a). After complete crack propagation, the contour of peak nominal stress exhibited a decay as one moved away from the crack surface, except around the original crack surface where material points

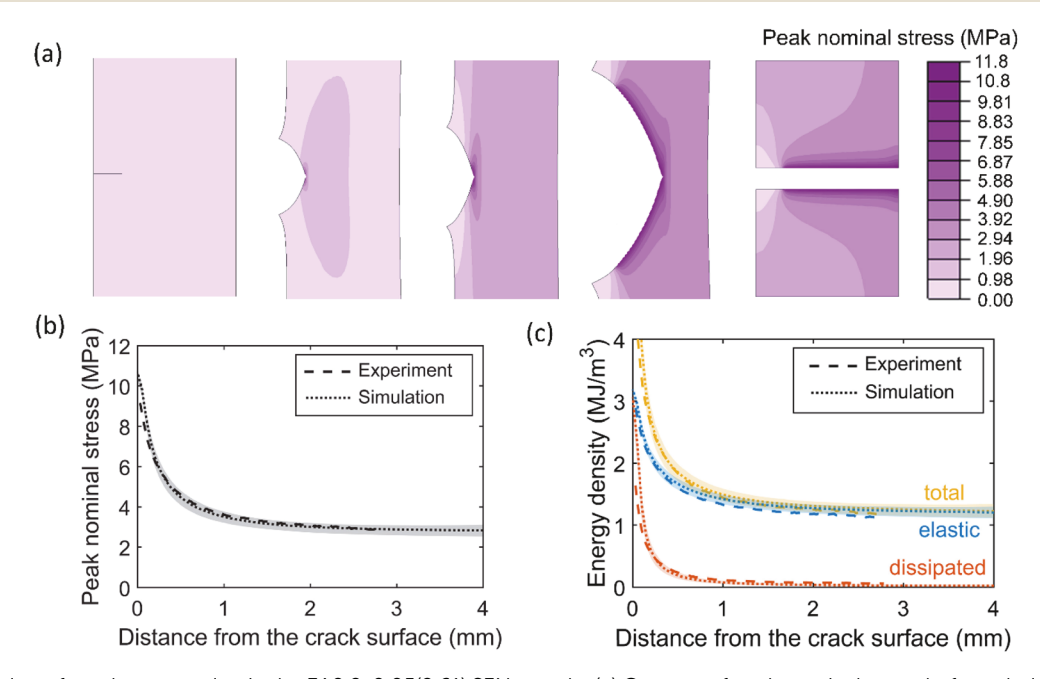


Fig. 5 FE simulation of crack propagation in the EA0.2-0.05(2.61) SEN sample. (a) Contour of peak nominal stress before, during and after crack propagation. (b and c) Comparison between simulation results and experimental data in terms of (b) the peak nominal stress and (c) the total, elastic and dissipated energy densities in the completely fractured SEN sample. The shaded regions represent ranges of the simulation results and the dotted lines represent the averages of simulation results.

did not experience as large loading as those around the newly created crack surface. Quantitative comparisons between the simulation results and the post-mortem analysis were made in Fig. 5b and c for the peak nominal stress and energy densities, showing excellent agreement. We also found that the stress maps plotted using the simulation results (Fig. S24†) resembled those measured by the mechanophore (Fig. 3c). The agreement between FE simulation and experimental data further supported the utility and validity of the stress history measurement using mechanophores.

Conclusion

We have conclusively demonstrated the potential of incorporating spiropyran mechanophore molecules in a soft polymer network to measure stress history. As previously reported the transformation of SP into MC by mechanical force can be used to quantify stresses during loading but we exploit here the reversible change of MC from an isomeric form (stable under load) to another isomeric form (stable in the unloaded state). This fast and reversible change is accompanied by a change in light absorption and hence to a change in color. By constructing a 3D color-stress map of the change in chromaticity from loading and unloading uniaxial tensile tests, we can attribute a unique color hue not only to the actual stress seen by the sample but also to the stress history (i.e. the maximum stress seen by the sample during the cycle). Since the color analysis can be done with a simple RGB camera, we used the stress color map to investigate the spatial stress distribution in the dynamic process of crack propagation analyzing the propagation of a crack and showing that even in a highly elastic material such as our MNE, the crack starts moving before the peak stress.

We further explored the possibility to obtain the maximum stress seen by each material point by performing a color analysis after failure due to crack propagation. From this chromaticity information we obtained the map of the maximum stress seen by each pixel near the crack and validated the measurement by finite element simulations.

Conflicts of interest

There are no conflicts to declare.

Acknowledgements

We gratefully acknowledge helpful discussions with Prof. Rint Sijbesma, Prof. Hugh R. Brown, Dr Artem Kovalenko and Dr Huan Zhang. This project has received funding from the European Research Council (ERC) under the European Union's Horizon 2020 research and innovation program under grant agreement AdG No 695351. Yinjun Chen has benefitted from a scholarship from the Chinese Scholarship Council. Rong Long acknowledge support from a U.S. National Science Foundation CAREER AWARD (NSF CMMI-1752449). All data needed to evaluate the conclusions in the paper are present in the paper and/or the ESI.† Additional data available from authors upon request.

References

- 1 (a) Y. Chen and R. P. Sijbesma, Macromolecules, 2014, 47, 3797-3805; (b) Y. Chen, A. J. Spiering, S. Karthikeyan, G. W. Peters, E. W. Meijer and R. P. Sijbesma, Nat. Chem., 2012, 4, 559-562; (c) J. M. Clough, C. Creton, S. L. Craig and R. P. Sijbesma, Adv. Funct. Mater., 2016, 26, 9063-9074. 2 (a) B. A. Beiermann, S. L. B. Kramer, P. A. May, J. S. Moore, S. R. White and N. R. Sottos, Adv. Funct. Mater., 2014, 24, 1529-1537; (b) D. A. Davis, A. Hamilton, J. Yang, L. D. Cremar, D. Van Gough, S. L. Potisek, M. T. Ong, P. V. Braun, T. J. Martinez, S. R. White, J. S. Moore and N. R. Sottos, Nature, 2009, 459, 68-72; (c) G. R. Gossweiler, C. L. Brown, G. B. Hewage, E. Sapiro-Gheiler, W. J. Trautman, G. W. Welshofer and S. L. Craig, ACS Appl. Mater. Interfaces, 2015, 7, 22431-22435; G. R. Gossweiler, G. B. Hewage, G. Soriano, Q. Wang, G. W. Welshofer, X. Zhao and S. L. Craig, ACS Macro Lett., 2014, 3, 216-219; (e) G. R. Gossweiler, T. B. Kouznetsova and S. L. Craig, J. Am. Chem. Soc., 2015, 137, 6148-6151; (f) K. Imato, T. Kanehara, T. Ohishi, M. Nishihara, H. Yajima, M. Ito, A. Takahara and H. Otsuka, ACS Macro Lett., 2015, 4, 1307-1311; (g) M. Li, Q. Zhang and S. Zhu, Polymer, 2016, 99, 521-528; (h) G. O'Bryan, B. M. Wong and J. R. McElhanon, ACS Appl. Mater. Interfaces, 2010, 2, 1594-1600; (i) H. Oka, K. Imato, T. Sato, T. Ohishi, R. Goseki and H. Otsuka, ACS Macro Lett., 2016, 5, 1124-1127; (j) M. J. Robb, T. A. Kim, A. J. Halmes, S. R. White, N. R. Sottos and J. S. Moore, J. Am. Chem. Soc., 2016, 138, 12328-12331; (k) Q. Wang, G. R. Gossweiler, S. L. Craig and X. Zhao, Nat. Commun., 2014, 5, 4899; (l) T. Wang, N. Zhang, J. Dai, Z. Li, W. Bai and R. Bai, ACS Appl. Mater. Interfaces, 2017, 9, 11874-11881; (m) Z. Wang, Z. Ma, Y. Wang, Z. Xu, Y. Luo, Y. Wei and X. Jia, Adv. Mater., 2015, 27, 6469-6474.
- 3 (a) R. Gostl and R. P. Sijbesma, Chem. Sci., 2016, 7, 370–375;
 (b) H. Li, R. Göstl, M. Delgove, J. Sweeck, Q. Zhang, R. P. Sijbesma and J. P. A. Heuts, ACS Macro Lett., 2016, 5, 995–998; (c) T. Wang, N. Zhang, K. Zhang, J. Dai, W. Bai and R. Bai, Chem. Commun., 2016, 52, 9679–9682.
- 4 (a) Y. Chen, H. Zhang, X. Fang, Y. Lin, Y. Xu and W. Weng, ACS Macro Lett., 2014, 3, 141–145; (b) X. Fang, H. Zhang, Y. Chen, Y. Lin, Y. Xu and W. Weng, Macromolecules, 2013, 46, 6566–6574; (c) G. Hong, H. Zhang, Y. Lin, Y. Chen, Y. Xu, W. Weng and H. Xia, Macromolecules, 2013, 46, 8649–8656; (d) S. Jiang, L. Zhang, T. Xie, Y. Lin, H. Zhang, Y. Xu, W. Weng and L. Dai, ACS Macro Lett., 2013, 2, 705–709.
- 5 (a) J. Li, T. Shiraki, B. Hu, R. A. Wright, B. Zhao and J. S. Moore, *J. Am. Chem. Soc.*, 2014, 136, 15925–15928; (b)
 J. Sung, M. J. Robb, S. R. White, J. S. Moore and N. R. Sottos, *J. Am. Chem. Soc.*, 2018, 140, 5000–5003.
- 6 (a) E. Ducrot, Y. Chen, M. Bulters, R. P. Sijbesma and C. Creton, *Science*, 2014, 344, 186–189; (b) P. Millereau, E. Ducrot, J. M. Clough, M. E. Wiseman, H. R. Brown, R. P. Sijbesma and C. Creton, *Proc. Natl. Acad. Sci. U. S. A.*, 2018, 115, 9110–9115.

Edge Article

- 8 J. Slootman, V. Waltz, C. J. Yeh, C. Baumann, R. Göstl, J. Comtet and C. Creton, *Soft Condensed Matter*, 2020.
- 9 S. Mzabi, D. Berghezan, S. Roux, F. Hild and C. Creton, *J. Polym. Sci., Part B: Polym. Phys.*, 2011, **49**, 1518–1524.
- 10 Y. Qi, Z. Zou, J. Xiao and R. Long, *J. Mech. Phys. Solids*, 2019, **125**, 326–346.
- 11 (a) G. Besnard, F. Hild and S. Roux, *Exp. Mech.*, 2006, **46**, 789–803; (b) F. Hild, A. Bouterf and S. Roux, *Int. J. Fract.*, 2015, **191**, 77–105.
- 12 Z. Xia, V. D. Alphonse, D. B. Trigg, T. P. Harrigan, J. M. Paulson, Q. T. Luong, E. P. Lloyd, M. H. Barbee and S. L. Craig, *Molecules*, 2019, 24, 524.
- 13 J. Park, Y. Lee, M. H. Barbee, S. Cho, S. Cho, R. Shanker, J. Kim, J. Myoung, M. P. Kim, C. Baig, S. L. Craig and H. Ko, Adv. Mater., 2019, 31, e1808148.

- 14 (a) R. S. Rivlin, *Philos. Trans. R. Soc.*, A, 1948, 241, 379–397;
 (b) A. P. S. Selvadurai, *J. Mech. Phys. Solids*, 2006, 54, 1093–1119.
- 15 (a) R. W. Ogden, Proc. R. Soc. London, Ser. A, 1972, 326, 565–584; (b) R. W. Ogden and D. G. Roxburgh, Proc. R. Soc. London, Ser. A, 1999, 455, 2861–2877.
- 16 A. N. GENT, Rubber Chem. Technol., 1996, 69, 59-61.
- 17 Y. Chen, C. J. Yeh, Y. Qi, R. Long and C. Creton, *Sci. Adv.*, 2020, **6**, eaaz5093.
- 18 (a) J. Hobley and V. Malatesta, *Phys. Chem. Chem. Phys.*, 2000,
 2, 57–59; (b) O. Kovalenko, Y. Lopatkin, P. Kondratenko and D. Belous, *Eur. Phys. J. D*, 2018, 72, 20.
- 19 H. Zhang, Y. Chen, Y. Lin, X. Fang, Y. Xu, Y. Ruan and W. Weng, *Macromolecules*, 2014, 47, 6783–6790.
- 20 E. Ducrot and C. Creton, *Adv. Funct. Mater.*, 2016, **26**, 2482–2492.
- 21 W. Qiu, P. A. Gurr and G. G. Qiao, *Macromolecules*, 2020, 53, 4090–4098.
- 22 C. J. Wohl and D. Kuciauskas, J. Phys. Chem. B, 2005, 109, 22186–22191.

Electronic Supplementary Material (ESI) for Chemical Science. This journal is © The Royal Society of Chemistry 2020

80309.

Fast Reversible Isomerization of Merocyanine as a Tool to Quantify Stress History in Elastomers

Yinjun Chen¹, C. Joshua Yeh¹, Qiang Guo², Qi Yuan², Rong Long² and Costantino Creton^{1*}

¹Laboratory of Soft Matter Science and Engineering, ESPCI Paris, Université PSL, CNRS,

Sorbonne Université, 75005 Paris, France

²Department of Mechanical Engineering, University of Colorado Boulder, Boulder, CO, USA

1. Synthesis of multiple network elastomers and characterization of mechanical properties

1.1 Synthesis of mechanochromic multiple network elastomers

The SP mechanophore was synthesized as previously reported¹ and the detailed procedure is shown in Scheme S1. SP diol was synthesized by the addition reaction of compound of 2 and 3, and then was functionalized with double bonds via the substitution reaction with methacryloyl chloride. Thus an SP-diene yellow powder was obtained and was used as a crosslinker in the polymerization of multiple network elastomers.

Scheme S1: The synthesis of the SP crosslinker

Single network (SN) materials were synthesized in the following way: 0.05 mol% SP and 0.15 mol% 1,4-butanediol diacrylate (BDA) crosslinker (relative to monomer) were dissolved into ethyl acrylate (EA) monomer with 1 mol% 2-hydroxy-2-methylpropiophenone (HMP) photo initiator. The mixture was then poured into a mold composed of a metal scaffold, a silicone spacer and two flat pieces of glass, and then polymerized 2 hours by UV exposure. As previously described², the single network acts as a filler network in multiple network elastomers and mainly controls the mechanical properties of the materials. To compare the evolution of the stress in a dynamic deformation process such as fracture for different materials, we also synthesized a different single network by increasing the total crosslinker concentration from 0.2 mol% to 0.5 mol% and keeping a constant SP concentration (0.05 mol%) relative to EA monomer. Using these two SNs as filler networks, varying families of materials were prepared by repeated swelling and polymerization steps with EA monomer. The composition of the matrix is the same as that previously reported with EA monomer and 0.01 mol% crosslinker. All the materials used in this article are shown in Table S1.

 Table S1: Various multiple network elastomers were synthesized for the quantification of stress

Polymer name	x-linker	SN wt%	C _{SP} mol%	λ_0	N _{poly}
	mol%				
EA0.5-0.05(1)	0.5	100	0.05	1	1
EA0.5-0.05(1.56)EA	0.5	26.5	0.05	1.56	2
EA0.5-0.05(2.23)EA	0.5	9.0	0.05	2.23	3
EA0.2-0.05(1)EA	0.2	4.4	0.05	2.84	1
EA0.2-0.05(1.70)	0.2	100	0.05	1	2
EA0.2-0.05(2.61)EA	0.2	20.2	0.05	1.70	3

x-linker represents the crosslinked density in the filler network of polymer materials. N_{poly} , Csp, and λ_0 are the total step number of polymerization, SP concentration and prestretch in the filler network.

1.2 Uniaxial tensile test

The multiple network elastomers (MNE) in Table S1 were used to perform uniaxial extension tests. Uniaxial extension experiments were performed on a standard tensile Instron machine (model 5565, fitted with a 100 N load cell). Samples with a dog-bone shape were used to carry out elongation tests with a stretch rate $\lambda = 0.05 \text{ s}^{-1}$ and the stretch was measured with a camera by recording the position of two black marks on the centers of the dog-bone samples. The stress-strain curves for various samples are shown in Figure S1.

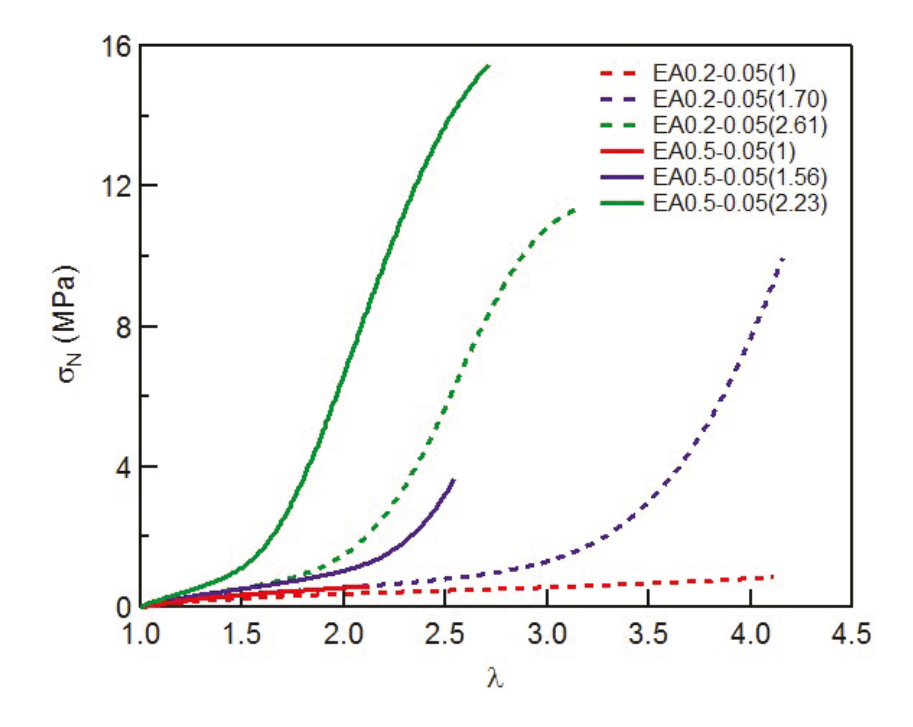


Figure S1: Stress-strain curves of the EA0.2-0.05 and EA0.5-0.05 families of samples

1.3 Step cyclic loading

Step cyclic loading were also performed on the EA0.2-0.05(2.61) and EA0.5-0.05(2.23) materials with a nominal stretch rate of 0.05 s^{-1} . The maximum strains λ ranged from 1.5 to 2.8 and the maximum stretch increased by 0.1 at every step as shown in Figure S2. An RGB camera (SENTECH: STC-MCS241U3V, Image sensor: SONY IMX174, cell size: $5.86 \,\mu m \times 5.86 \,\mu m$) was used to record the color change of the samples in step cyclic loading tests. All the frames extracted from the videos were used to do RGB analysis.

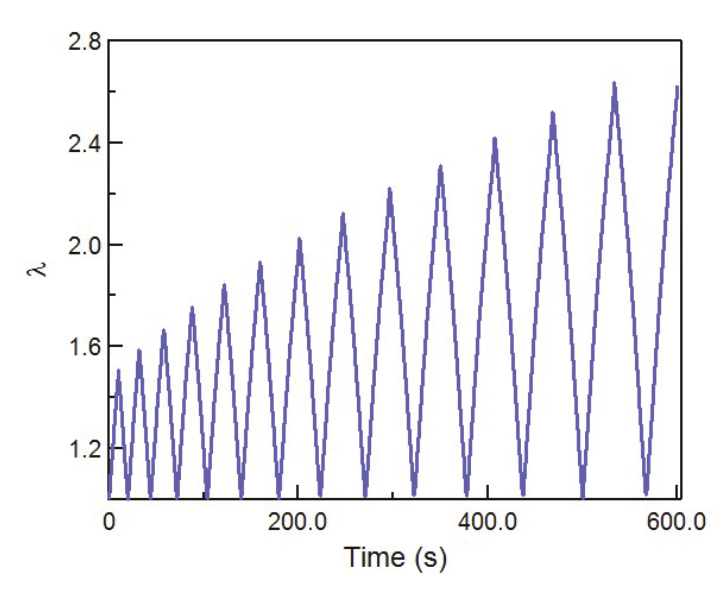


Figure S2: Stretch as a function of time during a step-cyclic loading test. The maximum stretch value of each cycle increased with each cycle by 0.1.

Figure S3a shows the stress-strain curves of EA0.5-0.05(2.23) and EA0.2-0.05(2.61). Both materials exhibit an obvious Mullins effect and a low viscoelasticity. When the stretch λ increases to $\lambda = 1.8$, the EA0.5-0.05(2.23) samples start to show an obvious hysteresis, validating the initiation of damage in the material. Accumulated hysteresis is calculated in step cyclic loading tests and shown in Figure S3b.

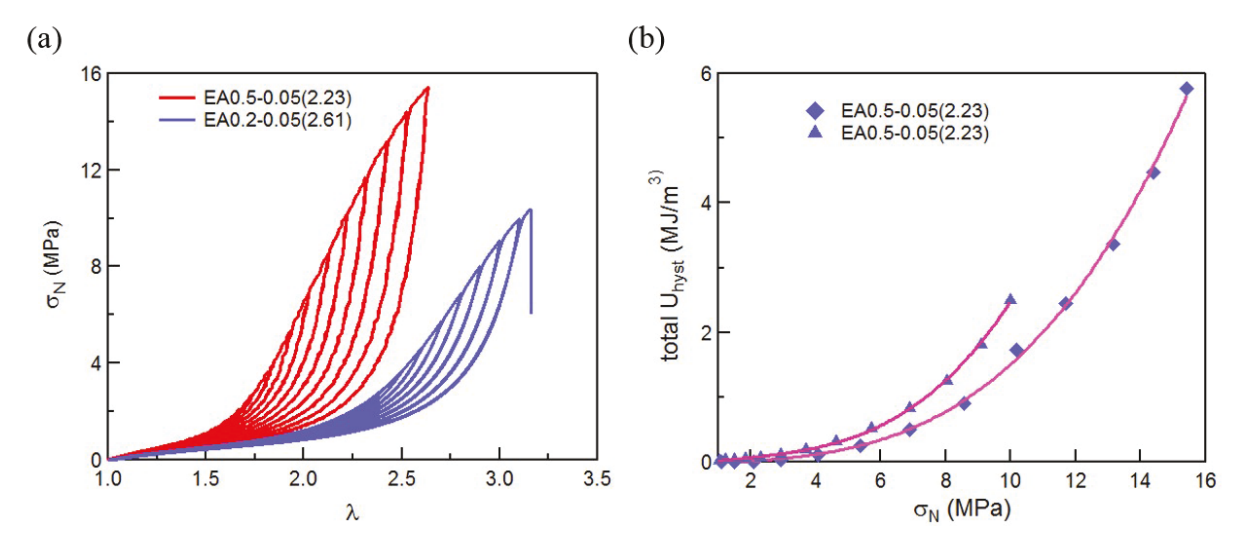


Figure S3: *Mechanical properties of EA0.5-0.05(2.23) and EA0.2-0.05(2.61) samples. (a) Stress-strain curve; (b) Accumulated hysteresis in step cyclic loading test.*

2. Color analysis

2.1. Image processing

Color correction and image processing applied to each video frame was carried out by using the same protocol outlined in the previous report².

2.2. Chromaticity

Chromaticity from color theory was used to quantify the color state of a pixel. The chromaticity of a channel in a pixel is defined as:

$$S_{ratio} = \frac{S}{\sum S},$$
 (S1)

where S is the generic representation of a color channel (R , G , or B). Chromaticity represents the relative contribution of a color channel relative to the total pixel intensity. The change in chromaticity, $^{\Delta S}_{ratio}$, relative to the beginning of an experiment can be tracked for each pixel and correlated with the applied nominal stress. Based on the chromatic changes for each color channel, the total color change, $^{\Delta T}_{ratio}$, can be defined as the Euclidean norm:

$$\Delta T_{ratio} = \sqrt{\sum \Delta S_{ratio}^2}.$$
 (S2)

Note that the color state of a pixel is sufficiently described by two chromatic descriptors, since the other chromatic descriptors can be determined based on Eq. (S1) and Eq. (S2).

2.3. Construction of the color-stress calibration map

The chromatic change of each color channel during a step-cyclic loading test of an EA0.2-0.05(2.61) sample can be visualized as a function of time in Figure S4a and as a function of nominal stress in Figure S4b. Specific chromatic descriptors (Total Chromatic change $^{\Delta T_{ratio}}$ and green chromatic change $^{\Delta G_{ratio}}$) were chosen for the stress-color map based on their high sensitivity for the loading and unloading step, respectively. Figure S5 shows the change in these chromatic descriptors during loading (blue line) and unloading from a specific maximum load (red lines). The loading of a virgin sample determines the level of SP activation into MC and during unloading and reloading, the chromatic coordinates retrace the same path, implying that the color change during unloading and reloading is a reversible process. If the chromatic change is plotted as a function of nominal stress, the red and blue chromatic changes do not show any obvious variation when the nominal stress is above 2.5 MPa in unloading and reloading. However, the green chromatic change rapidly decreases with nominal stress during unloading and increases during reloading as show in Figure S4b.

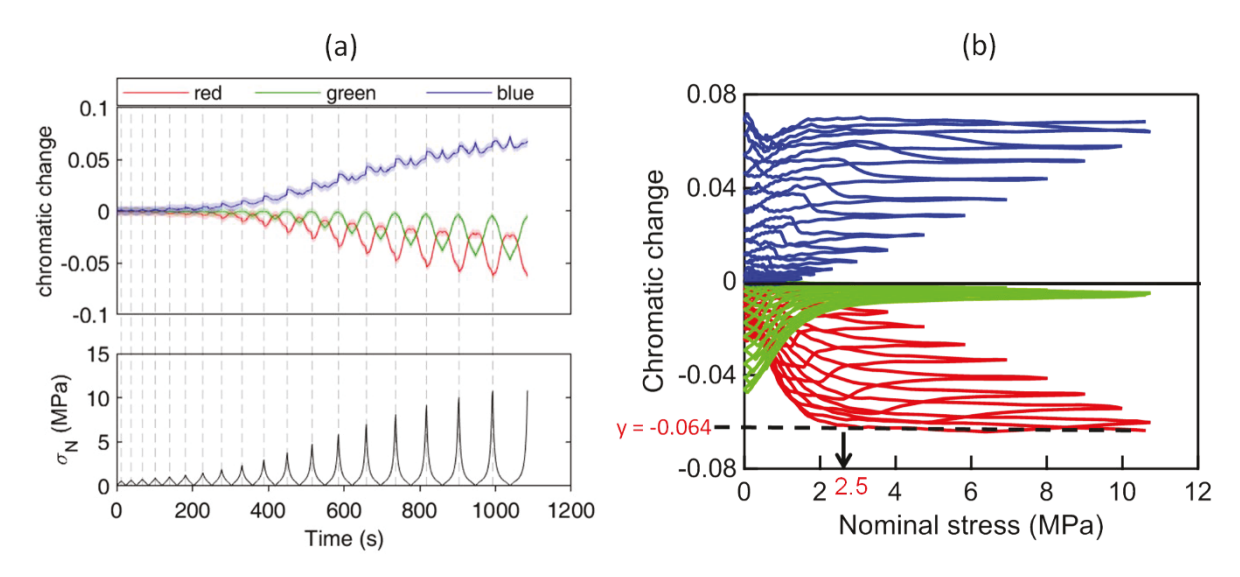


Figure S4: (a) The red, green, and blue chromatic changes of an EA0.2-0.05(2.61) sample undergoing step cyclic loading. The top and bottom figures share the same time axis. Dashed lines correspond to peak stress along the time axis. The transparent shaded regions in the

chromatic change evolution correspond to one standard deviation. (b) Red, Green and Blue chromatic changes as a function of nominal stress in step cyclic loading-unloading tests. The zero line (black solid line) corresponds to the initial color of the sample after correction of the background. The black dotted line at y = -0.064 and intersects the red chromatic change curve at the nominal stress above 2.5 MPa.

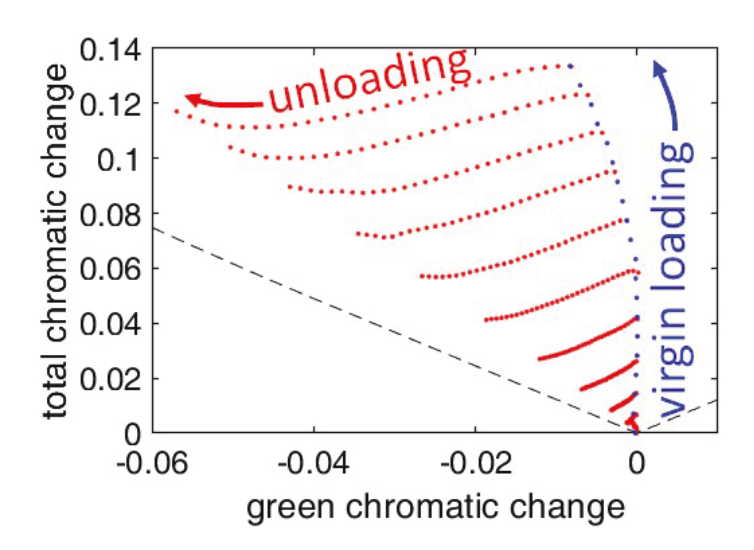


Figure S5: Chromatic map of an EA0.2-0.05(2.61) sample undergoing step cyclic loading. Blue dots represent measured chromatic changes while the sample was undergoing its first loading. Red dots represent measured chromatic changes while the sample was unloading and reloading. The dashed line corresponds to the boundary of physical meaningful chromatic coordinates.

A third order polynomial fit,

$$f(x) = p_1 x^3 + p_2 x^2 + p_3 x + p_4,$$
 (S3)

was used to describe the chromatic unloading paths obtained experimentally, as shown in Figure S6. The polynomial fit was performed using a total least-squares fitting method, in which the Euclidean distance between the experimental datapoints and the fitted line was minimized. This fitting approach accounts for variances in both the total chromatic and green chromatic changes. Also, to aid the interpolated prediction of unloading chromatic traces for a given applied peak stress, the polynomial fit was based on a normalized green chromatic change:

$$(\Delta G_{ratio})_{norm} = \frac{(\Delta G_{ratio}) - (\Delta G_{ratio})_{avg}}{(\Delta G_{ratio})_{std}},$$
 (S4)

where the subscripts, *avg* and *std*, denote the average and standard deviation of the experimental green chromatic change.

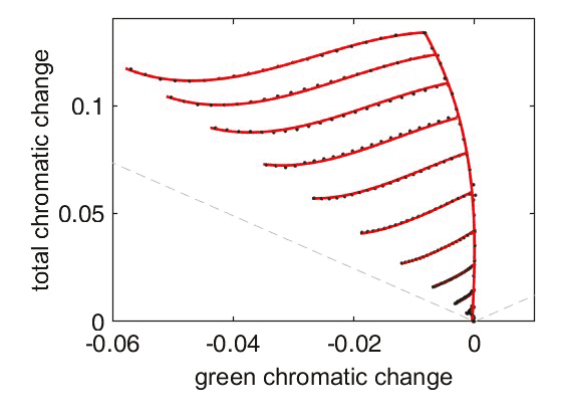


Figure S6: Chromatic map of an EA0.2-0.05(2.61) sample undergoing step cyclic loading. The black dots represent experimental datapoints. The grey dashed line corresponds to the boundary of physically meaningful chromatic coordinates. The solid red lines represent a third order polynomial fit based on a normalized green chromatic change.

To predict the unloading trace for a given peak stress along the loading curve, the third order polynomial coefficients used to fit the measured unloading chromatic curves were interpolated based on a fourth order polynomial fit as a function of the normalized green chromatic change when the sample was completely unloaded, as shown in Figure S7. Note that interpolation was not performed as a function of a given peak stress along the loading curve, since the peak stress of a pixel is not known a priori. Once the interpolated fitting coefficients were determined, the corresponding normalized green chromatic change was generated by spline interpolation of $(\Delta G_{ratio})_{avg}$ and $(\Delta G_{ratio})_{std}$ as a function of the green chromatic change of the completely unloaded sample, as shown in Figure S8. The interpolated fitting coefficients (p_1, p_2, p_3, p_3) and interpolated $(\Delta G_{ratio})_{avg}$ and $(\Delta G_{ratio})_{std}$ were used to construct the predicted unloading chromatic curves as shown in Figure S9.

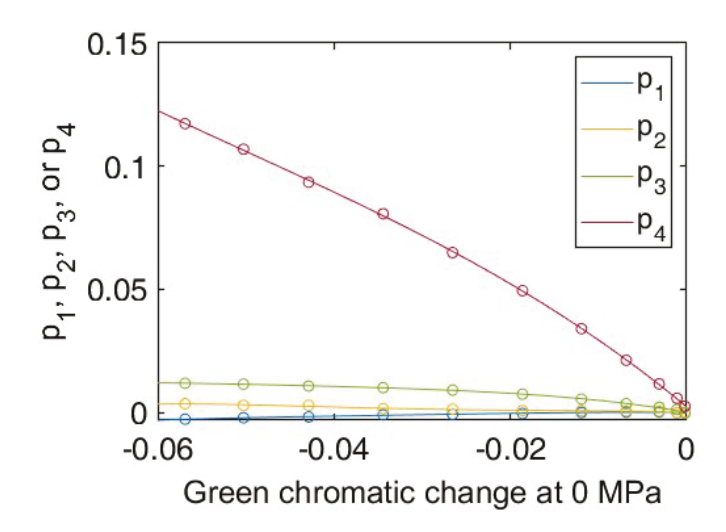


Figure S7: A fourth order polynomial fit of the third order polynomial fitting coefficients used to fit the experimental datapoints obtained from an EA0.2-0.05(2.61) sample undergoing step cyclic loading (see Figure 3). The fitting coefficients, p_1 , p_2 , p_3 , and p_4 correspond to the coefficients in Eq. (S3).

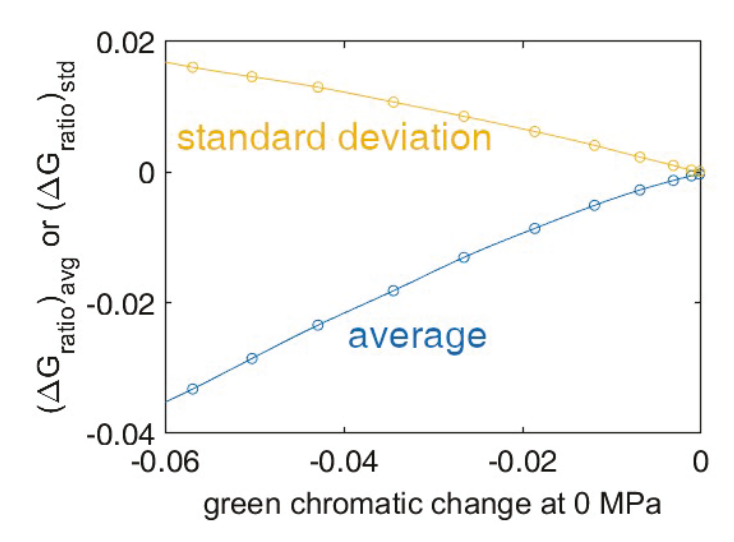


Figure S8: Spline interpolation of the average and standard deviation of the normalized green chromatic change (see Eq. (S4).

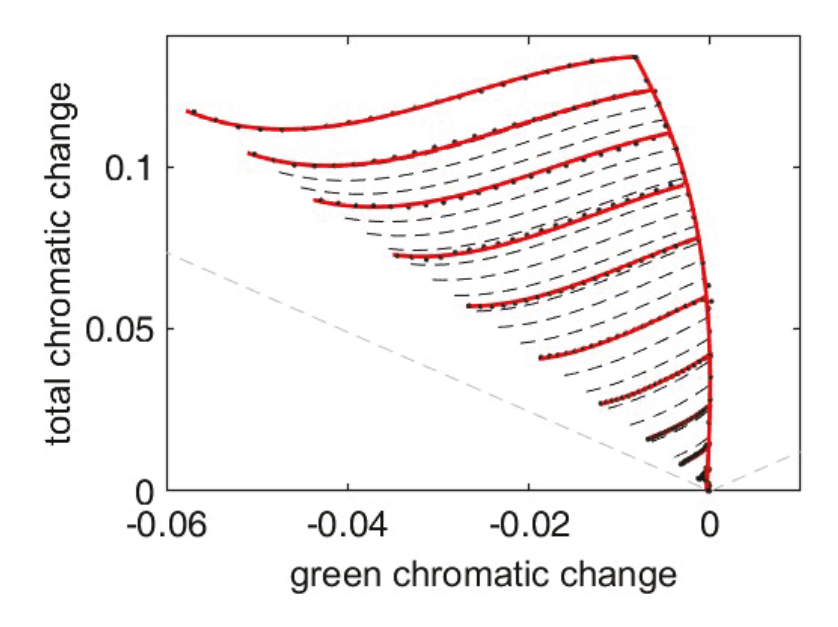


Figure S9: Chromatic map of an EA0.2-0.05(2.61) sample undergoing step cyclic loading. The black dots represent experimental datapoints. The solid red lines represent a third order polynomial fit based on a normalized green chromatic change. The black dashed lines are interpolated unloading chromatic traces. The grey dashed line corresponds to the boundary of physical meaningful chromatic coordinates.

The chromatic map in Figure S5 can be correlated to the applied nominal stress by overlaying isostress lines, as shown in Figure S10. To accomplish this, the unloading chromatic traces were fitted with the applied nominal stress, creating a 3D fit in the ${}^{\Delta T_{ratio}}_{-}{}^{\Delta G_{ratio}}_{-}{}^{\sigma_N}$ space that can be used to interpolate the corresponding chromatic coordinates based on a prescribed nominal stresses. Isostress lines were created by fitting a smoothing spline to the chromatic coordinates for each level of stress.

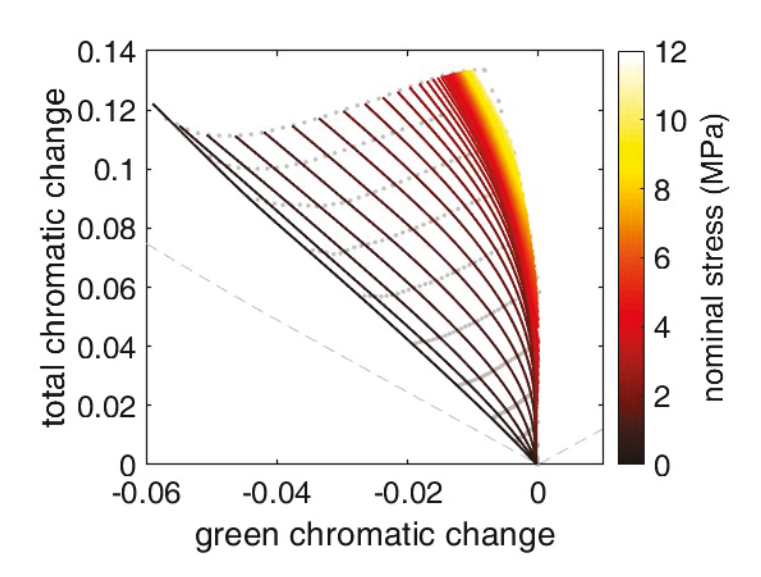


Figure S10: Chromatic-stress map of an EA0.2-0.05(2.61) sample undergoing step cyclic loading. Grey dots represent experimental datapoints (see Figure S5). Isostress lines are represented by colored solid lines that correspond to the color bar on the right. The dashed line marks the boundary of physically meaningful chromatic coordinates.

Application of the chromatic stress calibration map (3D color-stress map)

The dynamic process of crack propagation was taken as an example for the application of the chromatic stress calibration map. A flow chart summarizing how the stress is mapped and the peak stress is calculated are depicted in Figure S11.

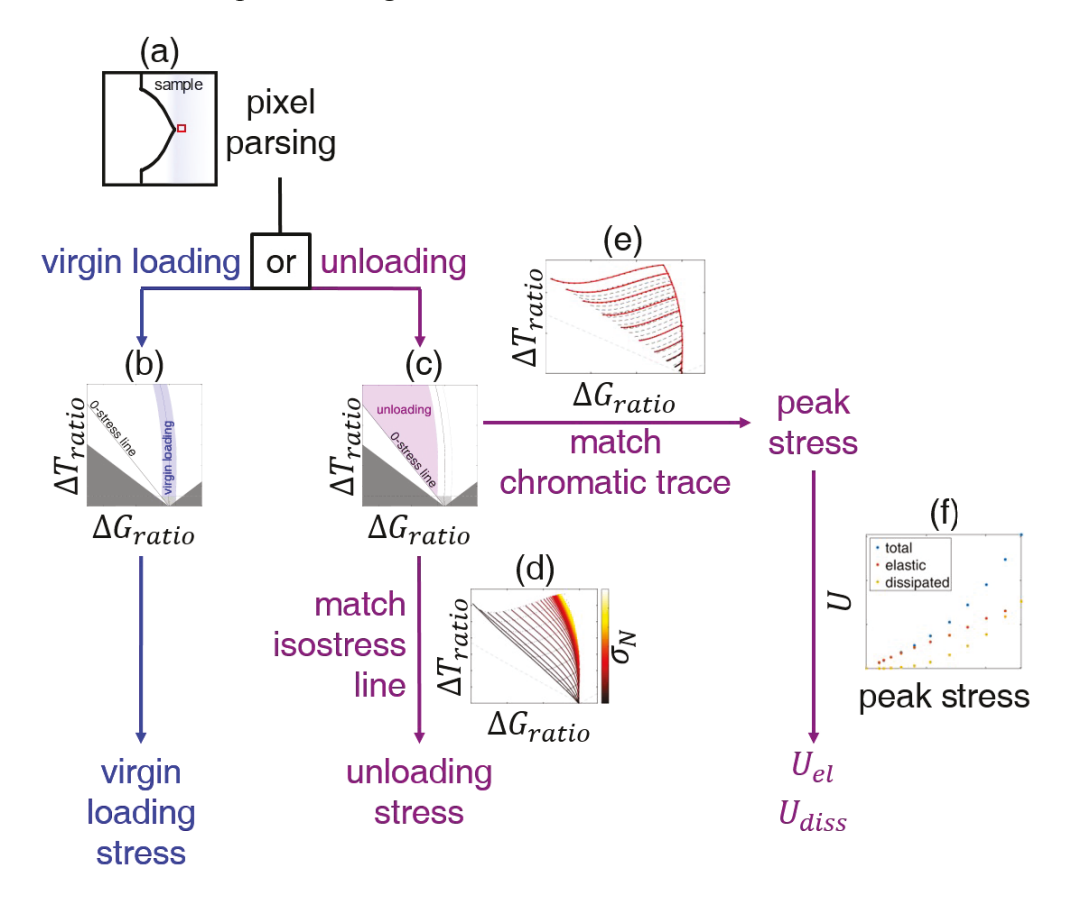


Figure S11: A diagram of how the images taken from the sample are analyzed. (a) A pixel in the sample region is selected for analysis. The pixel is parsed as virgin loading (b and Figure S13) or unloading (c and Figure S13)). Pixels parsed as unloading are associated with an unloading stretch by matching an unloading isostress line (d and Figure S10)). Also, unloading pixels are matched with an unloading chromatic trace (e and Figure S9) so that the peak nominal stress can be determined. The nominal peak stress is used to determine the elastic energy density, $^{U}_{el}$, and the dissipated energy density, $^{U}_{diss}$, by using a calibration curve (f and Figure S14))

Consider a rectangular, single edge notched fracture sample, in which the sample is pulled to failure. At the beginning of the experiment, a representative sample region in the image frame is used to estimate noise associated with sample surface roughness, surface impurities, etc. By observing histograms of the chromatic changes for each color channel and the total chromatic change in this region, as shown in Figure S12, a threshold value based on the 95% and 5% percentile of the total and green chromatic change, respectively, was established to differentiate signal from noise. The noise thresholds are also plotted on the chromatic map in Figure S13.

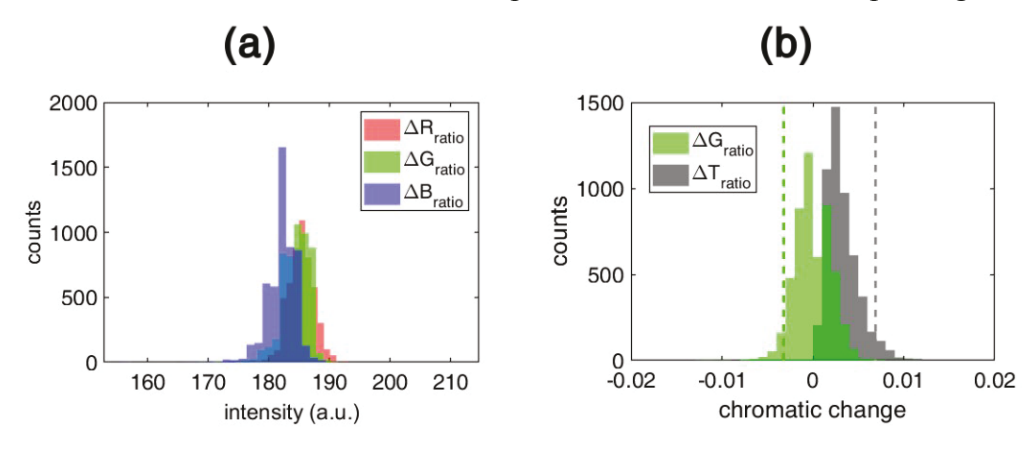


Figure S12: (a) Histograms of chromatic changes for each color channel. (b) Histograms of the total and green chromatic changes. The green and black dashed lines represent the 5% and 95% percentile in the green and total chromatic change distribution. $^{\Delta G}$ _{ratio} and $^{\Delta T}$ _{ratio} pairs that fall within the dashed lines were labelled as noise. Histograms were generated from the same representative sample region prior to loading.

As the fracture sample is stretched, the sample color and crack geometry will begin to change. A masking protocol (to mask the void created by the open crack) was used as described in Chen et al². Briefly, the image frame was guided by a binary thresholding method and subsequently modified manually, so that the front facing area of the sample was analyzed and that sample defects and regions exhibiting tri-dimensionality were ignored. The additional masking ensures that analysis is limited to regions where the sample thickness is relatively homogeneous.

Chromatic coordinates of the analyzed sample region are mapped onto the chromatic stress calibration map and are subsequently parsed as being under virgin loading or unloading, as shown in Figure S13. The boundaries used to parse the chromatic data were based on the absolute value of the 5% percentile of $^{\Delta G}_{ratio}$ of a representative sample region at the beginning of the experiment, herein referred to as $^{\sigma_{\Delta G}}_{ratio}$. The virgin loading region was defined by shifted loading curves along

the x-axis by ${}^{\pm}\sigma_{\Delta G_{ratio}}$. Datapoints that fall to the right threshold boundary were discarded in the analysis. Datapoints located in the purple region in Figure S13 were identified as pixels undergoing unloading and were associated with an unloading chromatic trace (see Figure S9) and an unloading isostress line (see Figure S10). Data falling within the blue region in Figure S13 were counted as pixels undergoing virgin loading and were correlated with a stress level along the virgin loading curve. Data association for virgin loading and unloading were performed using a MATLAB built-in function, knnsearch, which is a nearest neighbor algorithm.

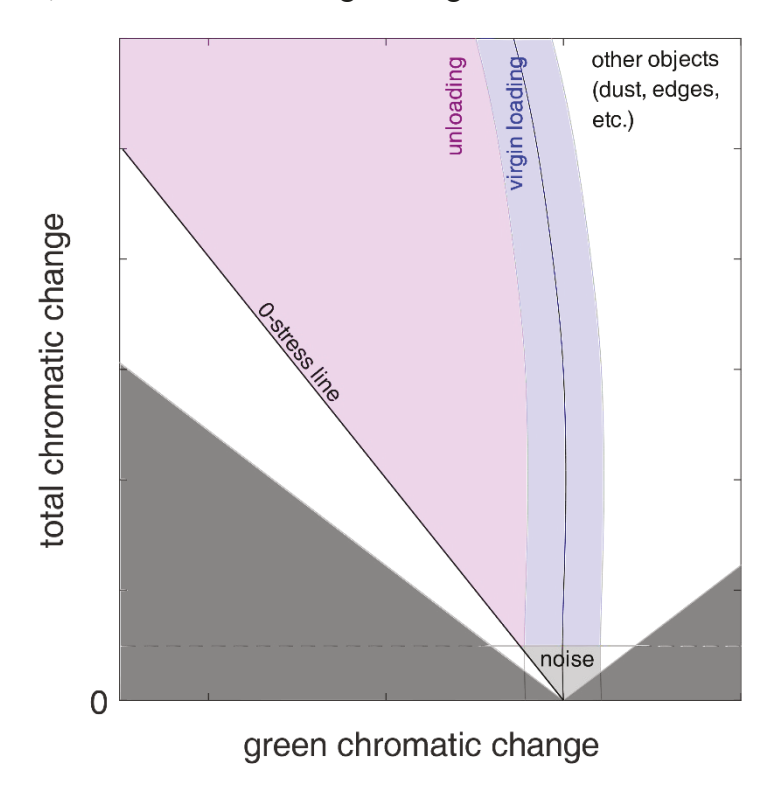


Figure S13: A schematic of how chromatic datapoints are parsed as virgin loading (blue region) or unloading (purple region). The white and light grey regions associated with noise, background, etc. were excluded from the analysis. The quasi-vertical grey lines that define the boundaries of the virgin loading region. The horizontal grey line marks the 95% percentile in the total chromatic change distribution prior to sample loading (see Figure S12b). The diagonal black line traces the isostress line when then same was completely unloaded. The dark grey areas represent unphysical chromatic coordinates.

For pixels matched with an unloading chromatic trace on the chromatic stress map, information on the loading history was deduced, such as the peak nominal stress, elastic energy density, and dissipated energy density. The peak nominal stress was determined by finding the intersection between the unloading and virgin chromatic traces. Based on the peak nominal stress, the

associated elastic and dissipated energy density was calculated from the stress-strain data of the step-cyclic loading experiment in uniaxial extension, as shown in Figure S14.

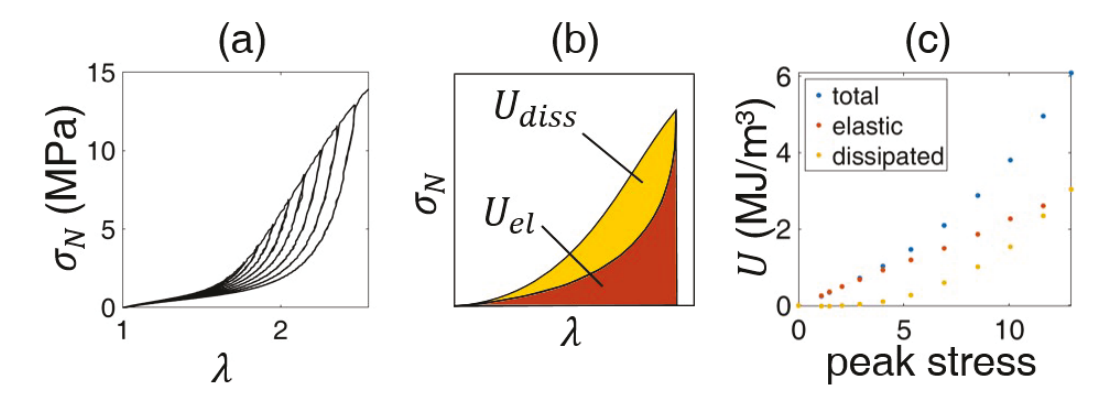


Figure S14: (a) Nominal stress and extension of a step cyclic loading test. (b) A schematic showing that the dissipated and elastic energy density is determined from the area between the loading-unloading curve and the area under the unloading curve, respectively. (c) A calibration curve between the total, elastic, or dissipated energy density and the peak nominal stress.

3. Post mortem analysis

Post mortem samples were obtained by carrying out a fracture test on a rectangular sample (5 mm wide, ~2 mm thick) with a single edge notch (~0.5 mm). The sample failed into two separate parts, which were used for color analysis. Based on the color change as a function of distance perpendicular from the crack edge, the stress history and concentration of activated mechanophore was determined.

3.1. Energy densities based on total color change

The peak stress, and energy densities (elastic and dissipated) were associated with the measured total chromatic change at 0-stress, $^{\Delta T}_{ratio}$, for each cycle taken from the step cyclic loading test. Calibration curves for both EA0.5-0.05(2.23) and EA0.2-0.05(2.61) are shown in Figure S15 and Figure S16, respectively. A linear fit was used to describe the correlation between the peak nominal stress and $^{\Delta T}_{ratio}^{\circ}$, elastic energy density ($^{U}_{el}$) and $^{\Delta T}_{ratio}^{\circ}$. To describe the correlation between the dissipated energy density, $^{U}_{diss}$, and $^{\Delta T}_{ratio}^{\circ}$, a 4th order polynomial fit was used. To account for errors in both the measured $^{\Delta T}_{ratio}^{\circ}$ and peak stress or energy density, a total least squares approach that minimizes the orthogonal distance between the datapoints and the fit was used.

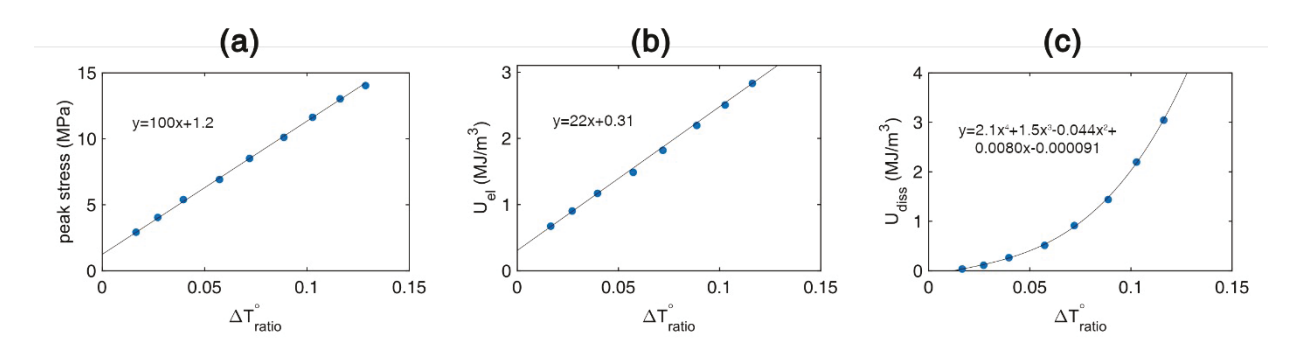


Figure S15: Calibration curves relating the peak nominal stress (a), elastic energy density, U_{el} , (b), and the dissipated energy density, U_{diss} , (c) to $^{\Delta T}_{ratio}$ for an EA0.5-0.05(2.23) sample.

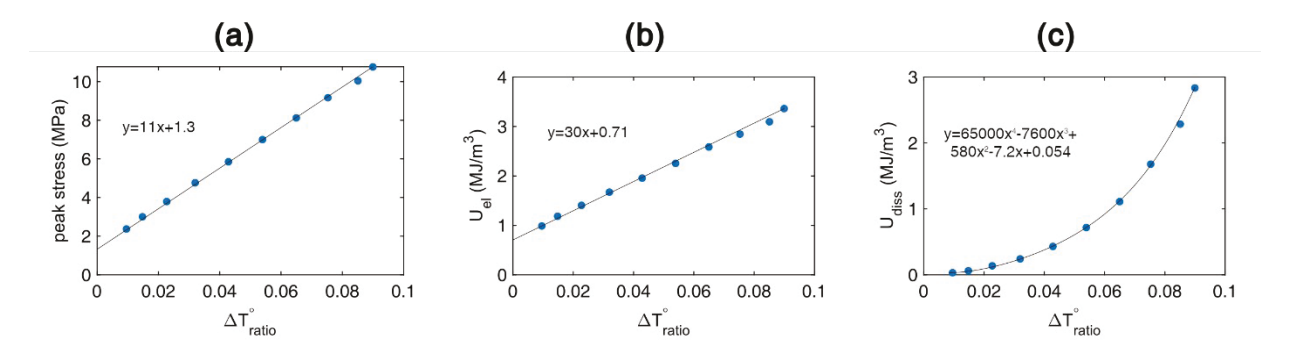


Figure S16: Calibration curves relating the peak nominal stress (a), elastic energy density, U_{el} , (b), and the dissipated energy density, U_{diss} , (c) to ΔT_{ratio} for an EA0.2-0.05(2.61) sample.

4. Stress maps

4.1 Maps of stress above 3 MPa

Stress maps around the crack tip were quantified by using the 3D color-stress map. In uniaxial step cyclic loading tests, when the stress increased to 3 MPa, the materials presented an obvious total hysteresis. In those materials, the irreversible hysteresis measured in uniaxial extension represents the damage in the polymer networks. Thus the regions where the stress exceeded 3MPa was mapped around the crack tip as shown in Figure S17. Before crack propagation the high stress almost concentrates in an area close to the crack tip, but during the slow advance of the crack the high stress region expands to the area far from the crack tip.

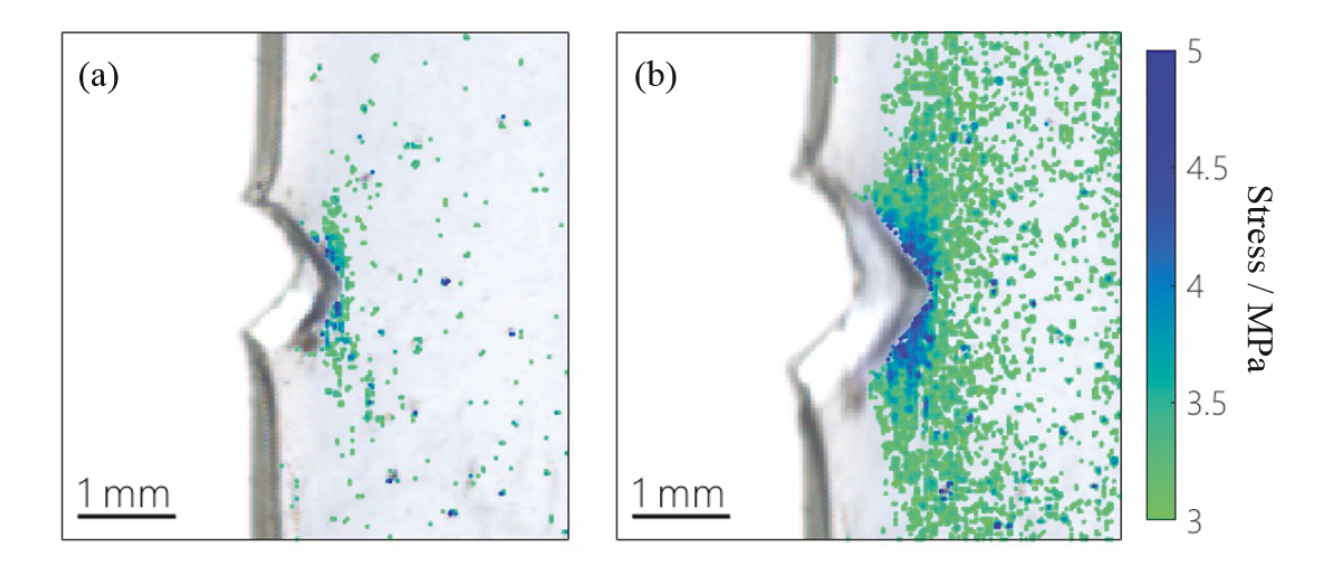


Figure S17: Stress map around the crack tip of EA0.5-0.05(2.23) samples before and during crack propagation.

4.2 Initiation of crack propagation

Before failure, materials with a notch normally display a slow and small advance of the crack followed by a rapid propagation resulting in the failure of materials. The color change of the materials around the crack tip during the slow advance stage are shown in Figure S18. From Figure S18 (a) to (f) it is observed that the crack surface increases gradually during the slow advance stage. The Figure S18 (a) and (f) are respectively corresponding to the original position of the slow and rapid propagation. In Figure S18 two small purple regions (partially unloaded) are symmetrically located near the crack tip. The evolution of stress distribution around the crack tip was quantified by using the 3D color-stress map. Figure S19 shows that the stress map evolution around crack tip prior to and during crack propagation.

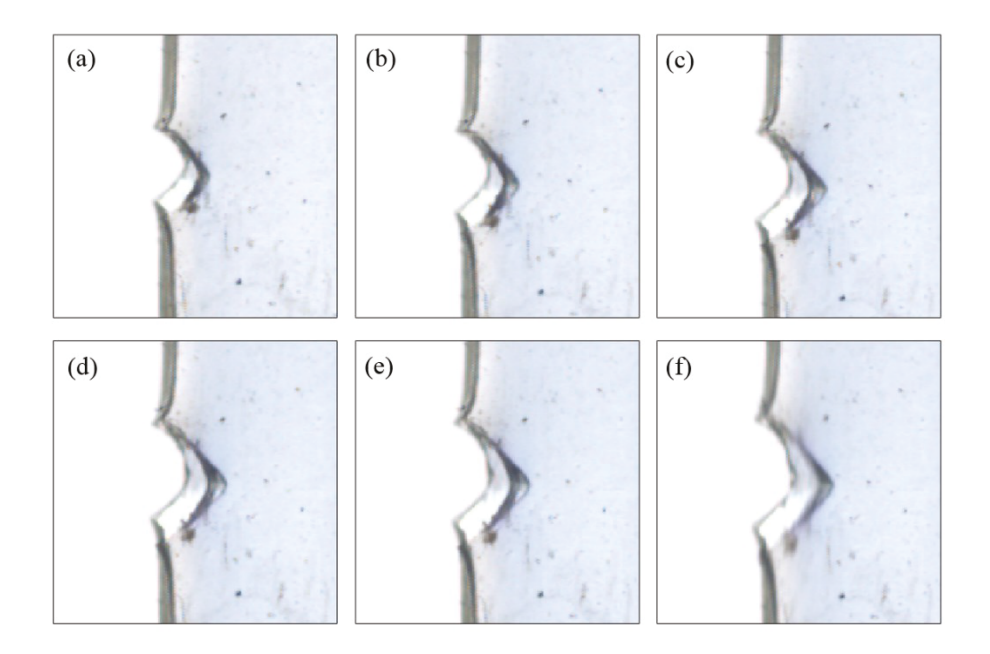


Figure S18: Original images of EA0.5-0.05(2.23) sample with a notch during the crack propagation

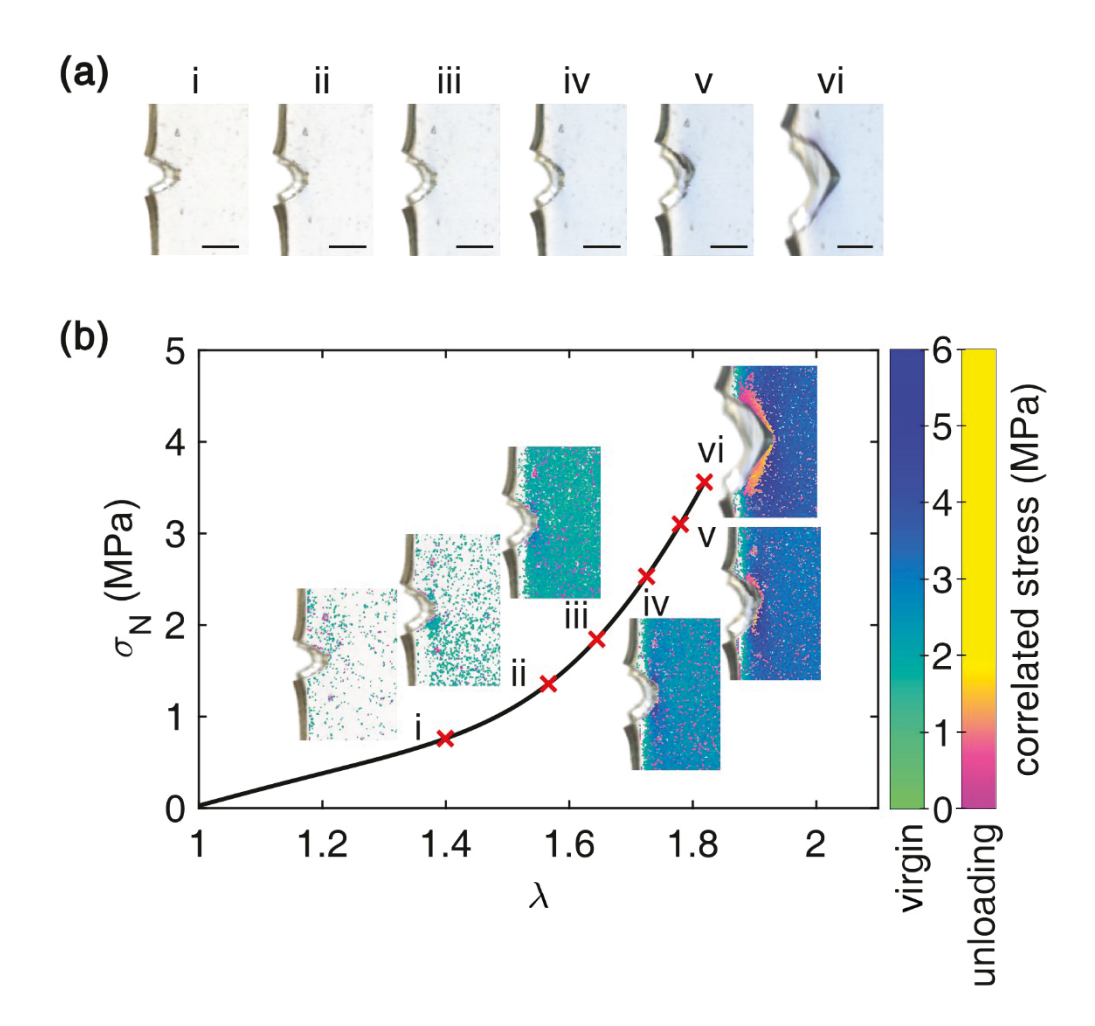


Figure S19: Stress maps of EA0.5-0.05(2.23) sample with a notch during the crack propagation. (a) The original images of EA0.5-0.05(2.23) sample with a single-edge notch showing two different color changes during a fracture test. The sample color changes from colorless to blue around the crack tip prior to the propagation and then some regions change from blue to purple during the crack propagation. The scale bar in the images represents 0.5 mm. (b) The stress map evolution is shown in (b).

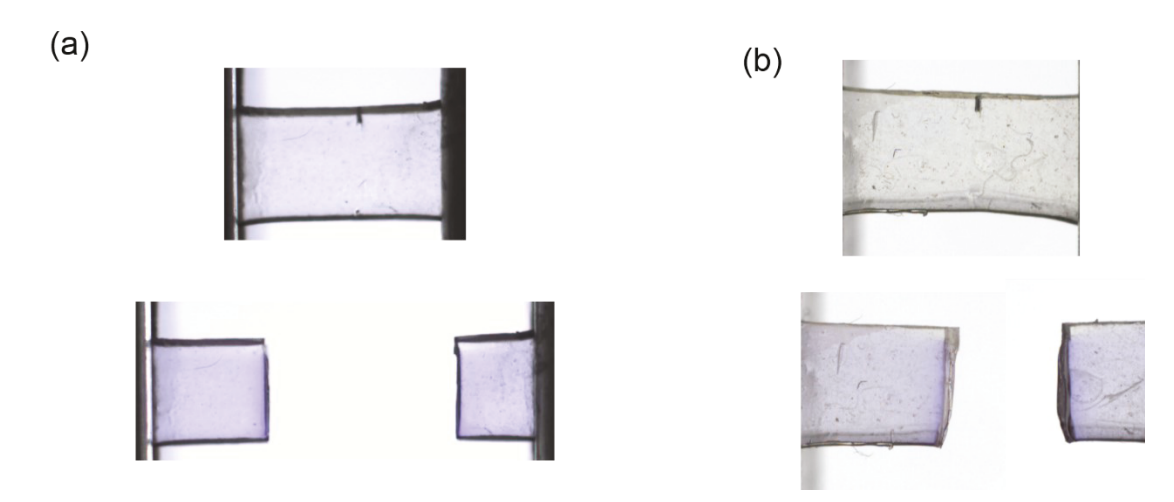


Figure S20: *Images of (a) EA0.5-0.05(2.23) and EA0.2-0.05(2.61) samples before and after fracture tests.*

Finite element simulation of crack propagation

An FE model to simulate the crack propagation in the SEN sample was built using the software ABAQUS (version 2019, Simulia, Dassault Systèmes, Providence, RI). The model consists of three main components: i) geometry, i.e., dimensions, mesh and boundary conditions; ii) constitutive model to capture the nonlinear, hysteretic stress-strain relations in the elastomer; iii) cohesive zone model on the projected path of crack propagation. These three components are detailed in the following.

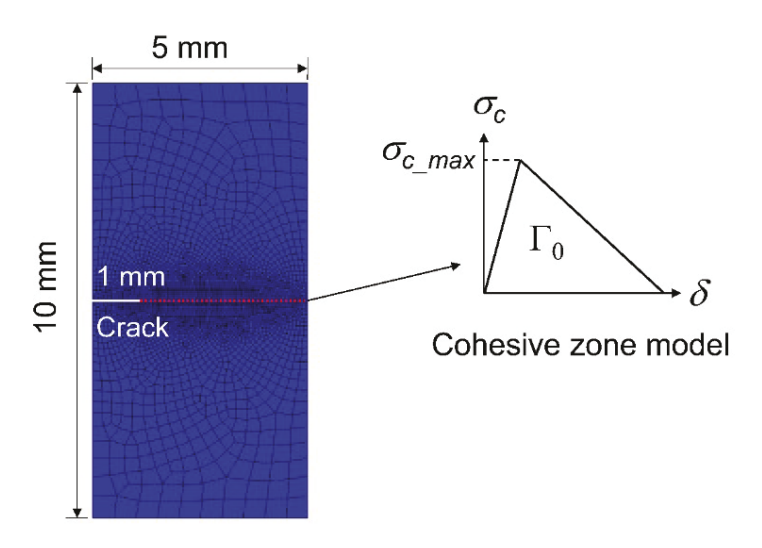


Figure S 21: FE model for simulating crack propagation in the SEN sample. A cohesive zone model with bilinear traction-separation law was implemented on the projected crack path (directly ahead of the original crack tip).

5.1 Model geometry

Dimensions of the FE model was set to be the same as the SEN sample (i.e. 5 mm \times 10 mm), as shown in Fig. S21. A 1mm crack was introduced on the left side of the model according to the experimental set up. To simulate crack propagation, a cohesive zone was introduced along the projected crack propagation path directly ahead the original crack tip. The top and bottom boundaries were separated by a displacement Δ along the vertical direction, and were subjected to zero displacement along the horizontal direction. The other boundaries (i.e., initial crack surfaces, the left boundary and the right boundary) were set to be traction free. Since the thickness of the SEN sample was much smaller than its lateral dimensions, we meshed the two-dimensional (2D)

FE model using plane stress elements (CPS4R). The mesh near the crack path were refined to improve accuracy with the smallest element size being 0.05 mm. Experimental observation suggested that crack propagation became unstable once the peak load was reached, which would lead to convergence difficulties for the implicit solver based on iterations. Therefore, the simulation was carried out using the explicit dynamic solver (ABAQUS/Explicit).

5.2 Constitutive model

The strain softening behavior of EA0.2-0.05(2.61), as shown in Fig. 2a of the main text, resembles the Mullins effect in filled rubber, which has been extensively studied in the literature. To quantitatively model the nonlinear inelastic behavior, we followed a phenomenological approach that uses one or more internal variables to capture the damage evolution under increasing strain³⁻⁶. First, we adopted the incompressible Arruda-Boyce model⁷, where the nominal stress tensor σ , also known as the first Piola-Kirchhoff stress tensor in the continuum mechanics literature, was given by the following equation:

$$\mathbf{\sigma} = \frac{\mu}{3} \frac{\sqrt{N}}{\lambda_{ch}} L^{-1} \left(\frac{\lambda_{ch}}{\sqrt{N}} \right) \mathbf{F} - p \mathbf{F}^{-T} , \qquad (S5)$$

where μ is the shear modulus at infinitesimal deformation, N is the average number of Kuhn segments on a chain, λ_{ch} is the equivalent stretch ratio on a chain, L^{-1} denotes the inverse Langevin function, \mathbf{F} is the deformation gradient tensor, and p is the Lagrange multiplier to enforce the incompressibility constraint. The equivalent chain stretch λ_{ch} was related to the macroscopic principal stretch ratios, λ_1 , λ_2 and λ_3 , through the 8-chain model:

$$\lambda_{ch} = \sqrt{\frac{\lambda_1^2 + \lambda_2^2 + \lambda_3^2}{3}} \,. \tag{S6}$$

In addition, we applied the following approximation by Cohen⁸ for the inverse Langevin function:

$$L^{-1}(y) = y \frac{3 - y^2}{1 - y^2}.$$
 (S7)

Under uniaxial tension, Eqs. (S5) and (S6) are reduced to

$$\sigma = \frac{\mu}{3} \frac{\sqrt{N}}{\lambda_{ch}} L^{-1} \left(\frac{\lambda_{ch}}{\sqrt{N}} \right) \left(\lambda - \frac{1}{\lambda^2} \right), \tag{S8}$$

and

$$\lambda_{ch} = \sqrt{\frac{\lambda^2 + 2/\lambda}{3}} \ . \tag{S9}$$

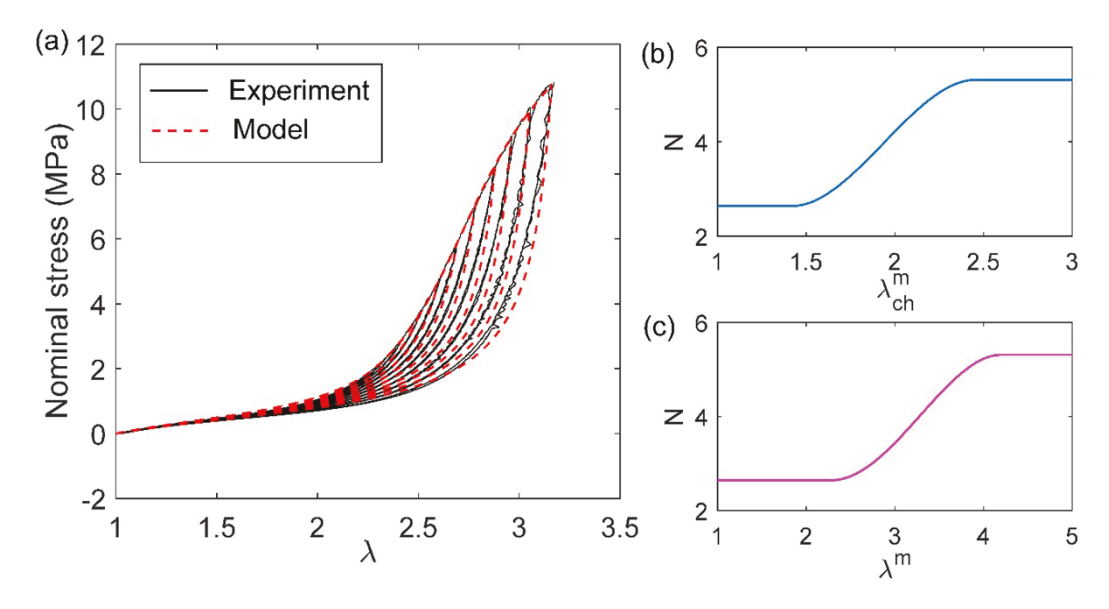


Figure S 22: Constitutive model for EA0.2-0.05(2.61). (a) Fitting the cyclic tension data using the constitutive model. (b-c) Evolution of the internal N with (b) the maximum equivalent chain stretch experienced in the history λ_{ch}^m and (c) the maximum stretch ratio experienced under uniaxial tension λ_{ch}^m .

In the Arruda-Boyce model, N is a material constant capturing the finite extensibility of the material. Here we treated N as an internal variable and allowed it to evolve with the loading history. Specifically, N was assumed to be a function of the maximum equivalent chain stretch experienced by the material, denoted as $\lambda_{ch}^m (\geq 1)$. The second law of thermodynamics dictates that N must be a non-decreasing function with λ_{ch}^m , otherwise it may result in negative energy dissipation over a loading cycle. By fitting the cyclic tension data of EA0.2-0.05(2.61) (see Fig.S22a), we found that $\mu = 0.3$ MPa and the following empirical function for $N(\lambda_{ch}^m)$:

$$N = \begin{cases} 2.64 & 1 \le \lambda_{ch}^{m} < 1.45 \\ -4.82817 \left(\lambda_{ch}^{m} - 1\right)^{3} + 13.5749 \left(\lambda_{ch}^{m} - 1\right)^{2} - 8.8499 \left(\lambda_{ch}^{m} - 1\right) + 4.32 & 1.45 \le \lambda_{ch}^{m} < 2.45 \\ 5.31 & 2.45 < \lambda_{ch}^{m} \end{cases}$$
(S10)

As illustrated in Fig.S22b, N monotonically increases with λ_{ch}^m when $1.45 \le \lambda_{ch}^m < 2.45$. The underlying physical mechanism is that damage in the swollen filler network (e.g. by chain scission) leads to an increase in the overall extensibility (i.e. increased N). Below the lower threshold ($\lambda_{ch}^m = 1.45$), damage is negligible and the material is elastic. Beyond the higher threshold ($\lambda_{ch}^m = 2.45$), the filler network is fully damaged and N no longer evolves. Under uniaxial tension, there is a one-to-one correspondence between λ_{ch}^m and the maximum stretch ratio experienced by the material: λ_{ch}^m . Therefore, N can also be plotted as a function of λ_{ch}^m in Fig.S22c, showing that the material model is elastic when $\lambda_{ch}^m < 2.34$ and becomes inelastic when $\lambda_{ch}^m = 1.45$ exceeds 2.34. The constitutive model described above was implemented in the FE simulation through a user subroutine VUMAT, i.e. a Fortran code specifying the stress-strain relations.

5.3 Cohesive zone model

We adopted a bilinear traction-separation law for the cohesive zone model as illustrated in Fig. S21a, and implemented in the FE model by introducing a layer of cohesive elements on the projected crack path (i.e. directly ahead of the crack tip). Since the crack propagation in the SEN sample was in Mode-I, the traction-separation law was in terms of the normal cohesive stress σ_c and the normal gap δ between the crack surfaces. Note that to accommodate the nonlinear effects due to large deformation, σ_c was defined as the normal nominal stress perpendicular to the crack path. The bilinear traction-separation law can be fully specified by three parameters: the intrinsic fracture energy Γ_0 (area enclosed by the traction-separation curve), the cohesive strength σ_{c_max} (maximum stress), and the initial stiffness K. Previous works in the literature⁹⁻¹⁰ suggested that the stiffness K did not affect the crack propagation simulation as long as it was sufficiently large. On the other hand, the simulation was sensitive to Γ_0 and σ_{c_max} . We leveraged the data of post-mortem analysis to determine these two parameters.

First, post-mortem analysis showed that the peak nominal stress near the crack surface was about 10MPa (see Fig.4c of the main text). This value was close to the nominal stress at break σ_m under macroscopic tension for EA0.2-0.05(2.61) (i.e., 11.3 MPa as listed in Table 1). The slight difference between the two values (i.e. 10 MPa versus 11.3 MPa) was attributed to the image resolution in the post-mortem analysis, since it posed a limitation accessing material points in the

vicinity of the crack surface. Therefore, the cohesive strength σ_{c_max} was set to be 11.3 MPa. Correspondingly, the initial stiffness K was set to be 8000 MPa/mm, which is sufficiently large since the separation δ related to the cohesive strength σ_{c_max} was only 1.3 μ m, much smaller than the smallest element size (= 0.05 mm).

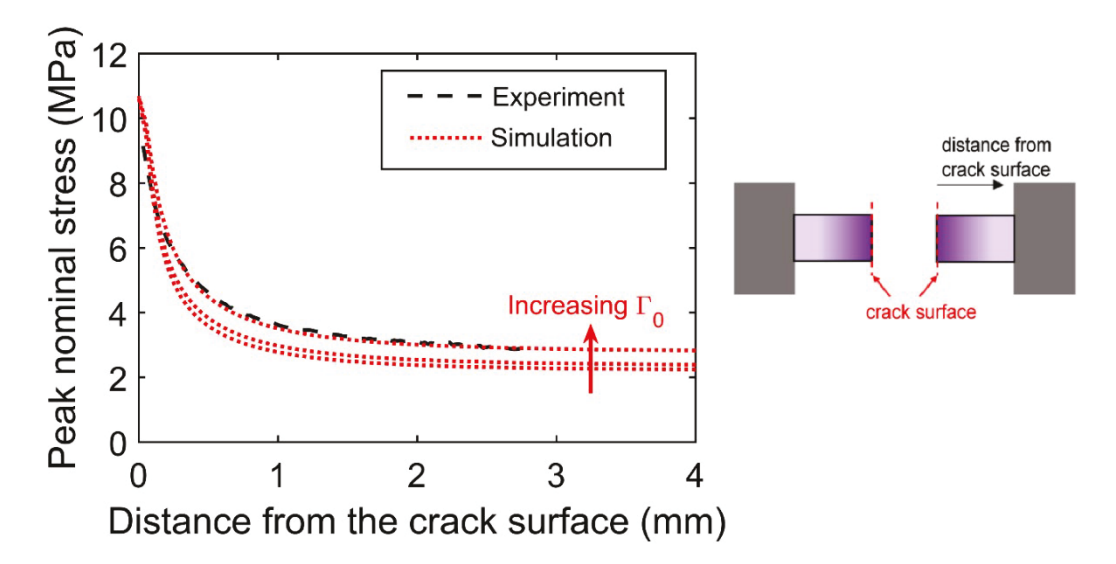


Figure S 23: Comparison between the experimental data of peak nominal stress distribution and simulation results based on three different Γ_0 (= 3.46 kJ/m², 3.77 kJ/m², 4.6 kJ/m²) and the same σ_{c_max} (= 11.3 MPa). The inset on the right shows a schematic of a completely fractured SEN sample and how the distance from the crack surface was defined.

Second, Γ_0 was determined by fitting the peak nominal stress distribution obtained from the postmortem analysis. Specifically, we ran FE simulations using different values of Γ_0 and extracted the peak nominal stress from each simulation. As demonstrated in our previous work², the experimentally measured nominal stress should be interpreted as the maximum principal nominal stress, which is equal to the maximum principal true divided by the corresponding principal stretch ratio. Following this definition, we calculated the maximum principal nominal stress and recorded its peak value along the deformation history, which was referred to as the "peak nominal stress". To compare with the post-mortem data, we extracted the peak nominal stress along 7 vertical paths located at 0.5 mm, 1mm, 1.5 mm, 2 mm, 2.5 mm, 3 mm, or 3.5 mm ahead of the original crack tip, respectively. Average of the peak nominal stress was plotted in Fig. S23 together with experimental data from the post-mortem analysis, showing that the case of $\Gamma_0 = 4.6 \text{ kJ/m}^2$ produced an excellent agreement with the experimental data. Using $\sigma_{c_max} = 10 \text{ MPa}$ and $\Gamma_0 = 4.6 \text{ kJ/m}^2$, we

computed the contours of peak nominal stress and the distributions of peak nominal stress and energy densities (i.e. total, elastic and dissipated) in after complete propagation, and plotted them in Fig. 5 of the main text. The energy densities were calculated assuming each material point experienced cyclic uniaxial tension during crack propagation, i.e. neglecting the effect of multi-axial deformation state near the crack tip. The shaded regions for the simulations in Fig. 5b and Fig. 5c represent the range of results on the selected 7 vertical paths.

The value $\Gamma_0 = 4.6 \text{ kJ/m}^2$ can be further justified. It is seen from Fig. 3c of the main text that the onset of catastrophic crack propagation for EA0.2-0.05(2.61) occurred at $\lambda = 2.32$. For SEN sample, the energy release rate G at a certain global stretch ratio λ can be calculated using the following equation¹¹⁻¹²:

$$G = \frac{6}{\sqrt{\lambda}} \psi(\lambda) c \,, \tag{S11}$$

where c=1mm is the initial crack length and $\psi(\lambda)$ is the work per unit volume required to stretch the material to λ under uniaxial tension. Using our constitutive model which provided an excellent fit to the loading curve (see Fig. S22), we found that $\psi(\lambda=2.32)=1.015\times10^6$ J/m³ by integrating the area underneath the uniaxial stress-stretch curve of loading. Plugging this value into Eq. (S11), we obtained that G=4 kJ/m² at the onset of catastrophic crack propagation, which is close to the fitted value of $\Gamma_0=4.6$ kJ/m². Strictly speaking, since bulk dissipation can further enhance the fracture energy in addition to Γ_0 9-10, 4 kJ/m² should be interpreted as an upper bound for Γ_0 and yet it is ~13% smaller than the fitted value of $\Gamma_0=4.6$ kJ/m². To explain this discrepancy, we note that Eq. (S11) was obtained for rubber obeying the Mooney-Rivlin or the neo-Hookean model 12-13. However, the EA0.2-0.05(2.61) elastomer exhibited a strong strain stiffening behavior (see Fig. S22b), implying that a correction factor may be needed in the application of Eq. (11) to our experiment.

5.4 Simulated stress maps

In Fig. S24, we plotted the global nominal stress versus stretch ratio curve obtained from the simulation. Also included were the simulated stress maps at 6 different stretch ratios, which well captured the unloading regions featured in Fig. 3c of the main text. Despite the excellent agreement between simulation results and the post-mortem data (see Fig. 5 of the main text), the FE model

slightly overestimated the stress and stretch at the onset of catastrophic crack propagation. This is attributed to the possible difference in the crack tip geometry: our model assumed an ideal 2D crack, while in the experiment non-ideal crack tip geometry (e.g. slightly tilted crack front or micro-branches at the initial crack tip) may result from the cutting process that introduced the crack.

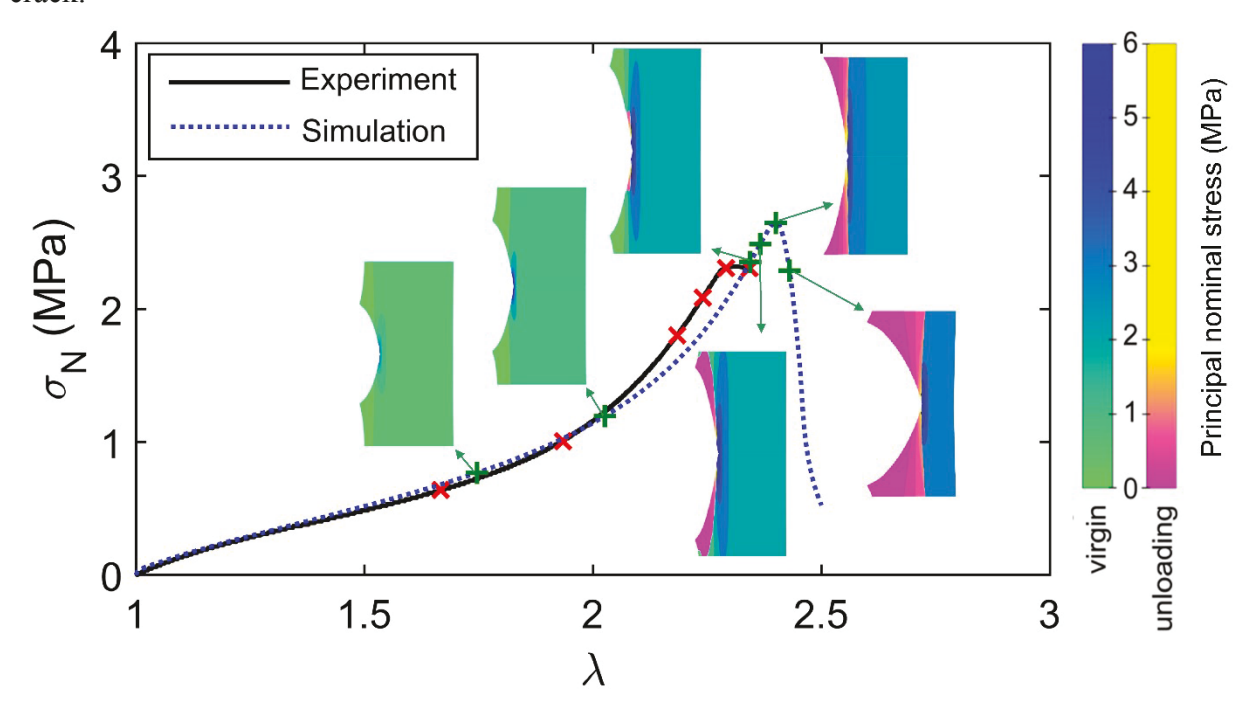


Figure S 24: Global nominal stress sN versus l for the SEN sample. The blue dotted line is obtained by the simulation and the black solid line represents the experimental data. Also included are the simulated stress maps corresponding to green symbols ("+") on the simulated stress-stretch curves. The red symbols ("x") on the experimental curve mark the points corresponding to the measured stress maps in Fig.3c of the main text (not shown here).

References

- 1. G. O'Bryan, B. M. Wong, J. R. McElhanon, Stress sensing in polycaprolactone films via an embedded photochromic compound. *ACS applied materials & interfaces* **2010**, *2* (6),1594-600.(10.1021/am100050v)
- 2. Y. Chen, C. J. Yeh, Y. Qi, R. Long, C. Creton, From force-responsive molecules to quantifying and mapping stresses in soft materials. *Science advances* **2020**, *6*,eaaz5093

- 3. M. Bacca, C. Creton, R. M. McMeeking, A Model for the Mullins Effect in Multinetwork Elastomers. *Journal of Applied Mechanics* **2017**, *84* (12).(10.1115/1.4037881)
- 4. X. Wang, W. Hong, Pseudo-elasticity of a double network gel. *Soft Matter* **2011**, 7 (18).(10.1039/c1sm05787a)
- 5. X. Zhao, A theory for large deformation and damage of interpenetrating polymer networks. *Journal of the Mechanics and Physics of Solids* **2012**, *60* (2),319-332.(10.1016/j.jmps.2011.10.005)
- 6. C. O. Horgan, R. W. Ogden, G. Saccomandi, A theory of stress softening of elastomers based on finite chain extensibility. *Proc. R. Soc. Lond. A* **2004**, *460*,1737-1754
- 7. E. M. Arruda, M. C. Boyce, A three-dimensional constitutive model for the large stretch behavior of rubber elastic materials. *J. Mech. Phys. Solids* **1993**, *41*,389-412
- 8. A. Cohen, A Padé approximant to the inverse Langevin function. *Rheol Acta* **1991**, *30*,270-273
- 9. Y. Qi, J. Caillard, R. Long, Fracture toughness of soft materials with rate-independent hysteresis. *Journal of the Mechanics and Physics of Solids* **2018**, *118*,341-364.(10.1016/j.jmps.2018.05.020)
- 10. T. Zhang, S. Lin, H. Yuk, X. Zhao, Predicting fracture energies and crack-tip fields of soft tough materials. *Extreme Mechanics Letters* **2015**, *4*,1-8.(10.1016/j.eml.2015.07.007)
- 11. A. Cristiano, A. Marcellan, B. J. Keestra, P. Steeman, C. Creton, Fracture of model polyurethane elastomeric networks. *Journal of Polymer Science Part B: Polymer Physics* **2011**, *49* (5),355-367.(10.1002/polb.22186)
- 12. H. W. Greensmith, Rupture of rubber. X. The change in stored energy on making a small cut in a test piece held in simple extension. *Journal of Applied Polymer Science* **1963**, 7,993-1002
- 13. O. H. Yeoh, Relation between crack surface displacements and strain energy release rate in thin rubber sheets. *Mechanics of Materials* **2002**, *34* (8),459-474